Ore Geology Reviews 187 (2025) 106935

Contents lists available at ScienceDirect

Ore Geology Reviews

journal homepage: www.elsevier.com/locate/oregeorev

Prospectivity mapping of high-purity barite mineralization in the Eastern Nigerian basement terrane using generalized algorithm-decoded thermal infrared data

Vandi Dlama Kamaunji [a,*], Ioan V. Sanislav [b], Dlama Zira Kamaunji [c], Dogara Obadiah Nkom [d], Hafizullah Abba Ahmed [c], Khaled M. Abdelfadil [e,f], Okopi Johnson Odumu [g], Daniel Wilberforce [c], Mabrouk Sami [e,h,**]

[a] State Key Laboratory of Geological Processes and Mineral Resources, School of Earth Sciences, China University of Geosciences, 430074 Wuhan, PR China
[b] College of Science and Engineering, James Cook University, Economic Geology, Townsville, QLD 4811, Australia
[c] Department of Geology, School of Physical Sciences, Modibbo Adama University of Technology, Yola P.M.B. 2076, Nigeria
[d] School of Economics and Management, China University of Geosciences, 430074 Wuhan, PR China
[e] Geosciences Department, College of Science, United Arab Emirates University, 15551 Al Ain, United Arab Emirates
[f] Geology Department, Faculty of Science, Sohag University, Sohag 82524, Egypt
[g] Department of Geology, Faculty of Natural Science, University of Jos, P.O. Box 2084, Jos 93001 Plateau state, Nigeria
[h] Geology Department, Faculty of Science, Minia University, 61519 El-Minia, Egypt

ARTICLE INFO

Keywords:
Thermal generalization method (TGM)
Multichannel algorithm
Barite prospectivity mapping
Thermal infrared (TIR)
Landsat-7 ETM+
Thermal radiation/water saturation

ABSTRACT

The Eastern Nigerian Basement Terrane hosts significant barite deposits critical for Nigeria's oil and gas industry, yet exploration remains limited to shallow artisanal mining that yield low-quality barite. This study presents a novel integration of Landsat-7 ETM + thermal infrared data and Shuttle Radar Topography Mission (SRTM) elevation data with the Thermal Generalization Method (TGM), a multichannel algorithm that transforms TIR-SRTM data into 3D thermodynamic models. Using algebraic-geometric transformations and algorithms including generalization (G), automatic identification of cell-block structure (AICDS), litho-temperature (LT), vertical temperature (VT), first/second Vertical Derivatives (IVD, 2VD), the method delineates high-purity barite mineralization at depths surpassing typical artisanal operations. Seasonal analysis quantified a 17 % drop in mean surface thermal radiation (10.42 to 8.67 W $m^{-}2$) and a 37 % rise in mean surface water saturation (0.46 to 0.63), showing a strong negative correlation ($r = -0.72$) that confirms seasonal heat-fluid coupling enhances mineralization potential at depth. TGM analysis identified two potential barite fields (PBF1 and PBF2) in the Mayo-Belwa and Jada-Ganye basement terranes, representing substantial, previously unrecognized high-grade targets within Nigeria's estimated 22 Mt barite reserves. These fields are characterized by dominant NNE-SSW lineaments and NW-SE stresses interact, with subordinate NNE-SSW stresses enhancing permeability through localized deformation, creating structural/thermochemical fluid pathways. PBF1 (Taso-Tola deposits), hosted in a deflection zone dominated by granite-gneisses, shows strong thermal anomalies ($\nabla T > 0.5$ K/m; $\partial 2T/\partial z2 < -0.3$ K/m2), indicative of exothermic barite precipitation at temperatures of 60–80 °C. Economic mineralization occurs along ENE lineaments at 180–300 m depth ($\Delta T = 1.2$ K, signal-to-noise ratio [SNR] 2000:1), with 70–90 % water saturation. These anomalies exceed Landsat's thermal resolution threshold by > 3 orders of magnitude, providing a robust, deterministic confidence framework. The Taso sector shows sharp thermal boundaries ($\partial T/\partial z > 0.6$ K/m) along 540 m fractures, whereas Tola's mineralization persists to 1,200 m ($\Delta T = 0.3$ K, SNR 2700:1) beyond optimal mineralization depths. PBF2, hosted in syn- to post-tectonic granites within zones of intense uneven uplift, exhibits subdued thermal signatures (40–60 °C) and moderate water saturation (50–70 %). NW–SE compression generates ENE uplift blocks controlling mineralization: Yebbe extends 610–750 m (60–300 m), Zeibei is vertically reoriented below 240 m, and Ngurore exhibits propeller geometry (870–780 m). High thermal gradients ($\nabla T > 0.7$ K) and water saturation ($W > 0.3$) favour barite deposition at 60–300 m depth, controlled by NNW-trending faults, although deeper anomalies ($\Delta T = 0.08$ K at 1,800 m) lie beyond viable exploitable limits.

* Corresponding author.
** Corresponding author at: Geosciences Department, College of Science, United Arab Emirates University, 15551 Al Ain, United Arab Emirates.
E-mail addresses: vandikamaunji@cug.edu.cn (V.D. Kamaunji), mabrouksami@uaeu.ac.ae (M. Sami).

https://doi.org/10.1016/j.oregeorev.2025.106935
Received 10 June 2025; Received in revised form 4 October 2025; Accepted 8 October 2025
Available online 20 October 2025

Both systems demonstrate barite deposition controlled by NW-SE compressive stress. TGM-decoded TIR identifies barite mineralization at optimal exploitable depths (60–300 m), overcoming artisanal mining limits (<15 m) and enabling the targeting of high-purity, API-compliant reserves vital to Nigeria oil and gas sector.

1. Introduction

Barite is critical for oil/gas drilling to stabilize wellbores (Basfar et al., 2025; Yang et al., 2025), yet Nigeria's 22.30 Mt reserves (Afolayan et al., 2021; Ebunu et al., 2021; NGSA, 2011) often fail API Spec 13A standards due to shallow mining (≤20 m), yielding impure barite (3.8–4.1, below the required 4.5 (Ciullo, 1996), necessitating imports for its oil/gas industries (O'Driscoll, 2017; Otoijamun et al., 2021). High-purity barite typically comes from deeper deposits—e.g., Nevada (200–350 m, SG 4.25–4.4; USGS, 2021), Sichuan (300–500 m, SG 4.3–4.6; Zou et al., 2016), and Morocco (40–500 m; Essalhi et al., 2016), where reduced oxidation preserves quality (Hanor, 2000; Yao et al., 2022; Moles et al., 2024). Thus, transitioning from artisanal shallow mining to mechanized deep extraction (>100 m) is essential for Nigeria's barite deposits to meet API purity standards. Remote sensing technologies, especially thermal infrared (TIR) and satellite structural analysis, effectively map mineral resources by detecting thermal anomalies, fluid saturation, and tectonic heat transfer (Wang et al., 2024; Amraoui et al., 2025; Li et al., 2025). Advances in emissivity-corrected land surface temperature (LST) analysis and geothermal algorithms have improved mineralization detection at regional scales (Mahboob et al., 2024; Madani & Said, 2024; Sary, 2024; Zhao et al., 2024). For Nigerian barite exploration, enhanced geospatial processing is needed to resolve deep structures and mineral signatures.

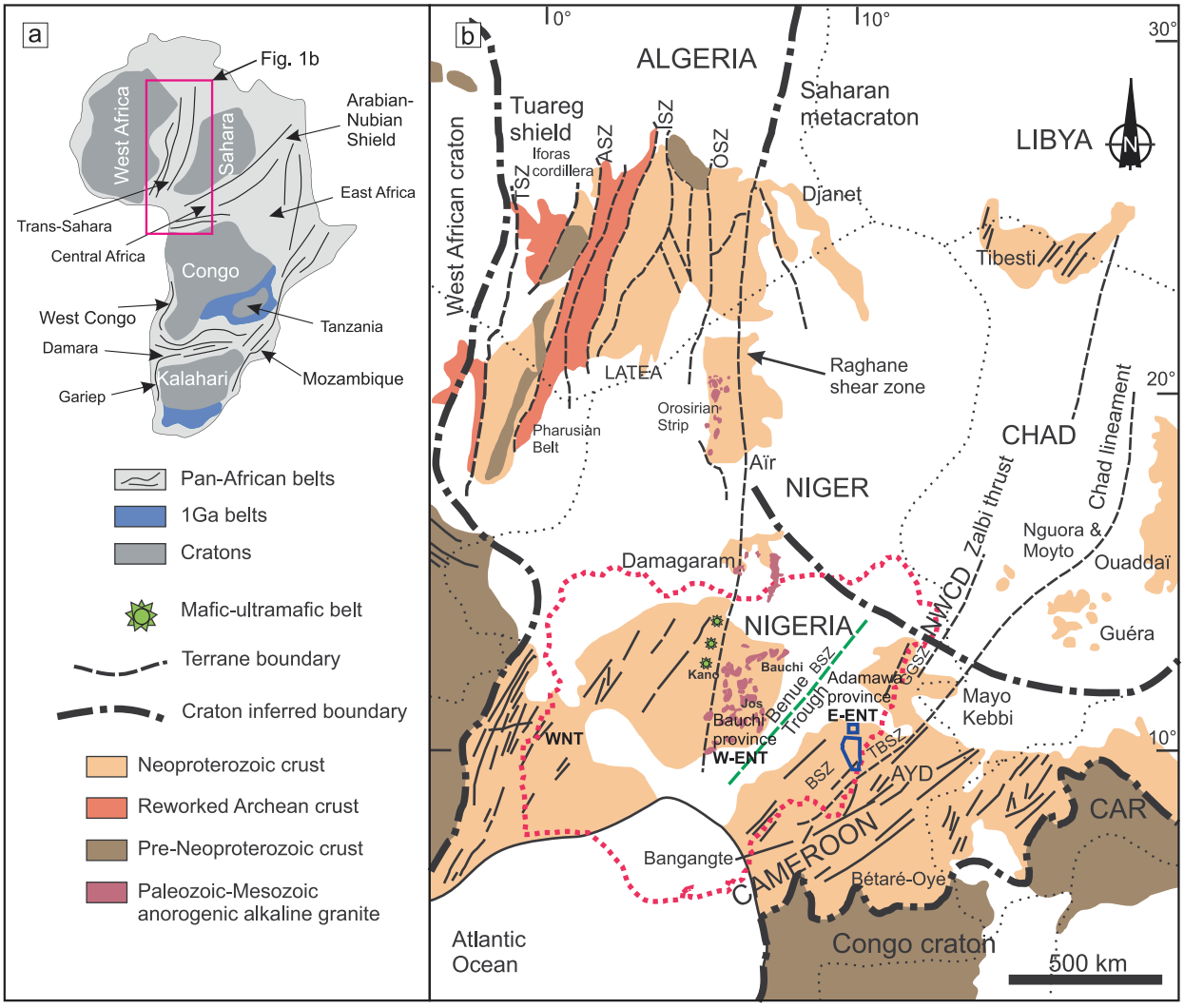

Fig. 1. (a) The geodynamic context of the Pan-African orogenic belts (Shellnutt et al., 2017); (b) regional geological map of the Trans-Saharan to Central Africa orogenic belts showing the major terranes (modified from Shellnutt et al., 2018). The Tuareg Shield is updated from Liégeois (2019) and includes four mega shear zones: the Tilemsi shear zone (TSZ), the Adrar shear zone (ASZ), the Iskel shear zone (ISZ), the Ounane shear zone (OSZ), and the Raghane shear zone (RSZ). The Raghane shear zone, which marks the boundary between the Western Nigeria Terrane (WNT) and Eastern Nigeria Terrane (ENT), is considered a potential suture zone (Ferré et al. 2002; Toteu et al., 2004). The Benue Trough Shear Zone (BSZ) is a hypothetical transcurrent shear zone buried by the Benue Trough that separates the ENT into the West-Eastern Nigeria Terrane (W-ENT) and East-Eastern Nigeria Terrane (E-ENT). The strong positive Bouguer anomaly in Chad is the southern extension of the Tcholliré–Banyo shear zone (TBSZ) (Penaye et al., 2006). The Zalbi tectonic zone comprises the Balché shear zone (BSZ) and Zalbi thrust shear zone (Pouclet et al., 2006). The Gode–Gormaya shear zone (GGSZ) marks the boundary between the E-ENT domain and NW Cameroon domain (NWCD). LATEA = Laouni-Azroun'Fad-Tefedest-Egéré-Aleksod, MKD = Mayo Kebbi domain, AYD = Adamawa-Yadé domain, CAR = Central African Republic.

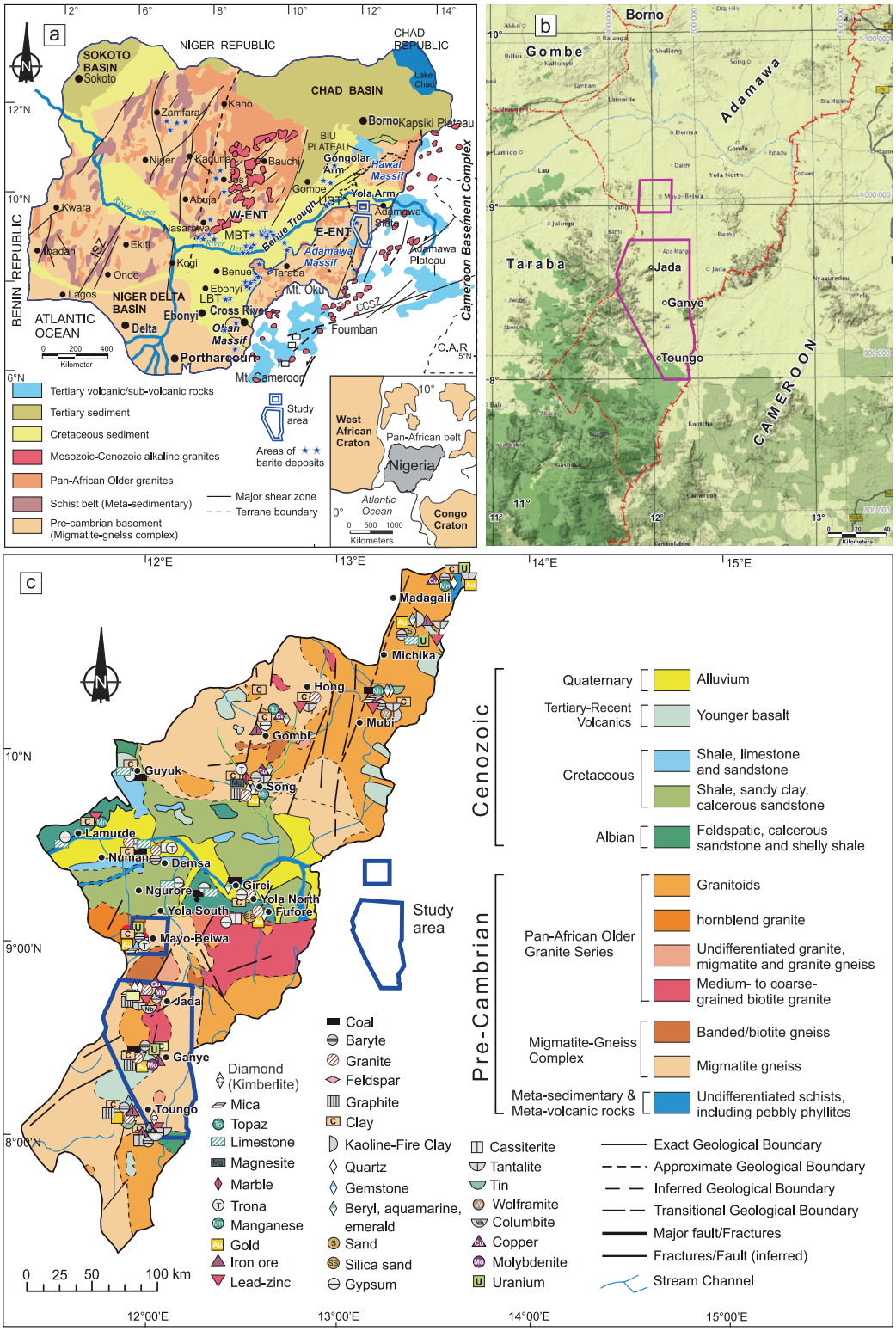

Fig. 2. (a) Geological map of Nigeria showing the study area within the Eastern Nigerian Basement Terrane (ENT), including the distribution of barite occurrences and major Pan-African-aged faults and shear zones (modified from Ngako et al., 2006; Obaje, 2009). The distribution of barite (indicated by blue stars) is from Ebunu et al. (2021). The fault and shear zone trends are predominantly NE–SW, NNE–SSW, E–W, ENE–WSW and NW–SE.. CCSZ: Central Cameroon Shear Zone (also referred to as Foumban Shear Zone); KSZ: Kaltungo Shear Zone; ISZ: Ifewara Shear Zone. Faults/shear zones in Nigeria are compiled from Rahaman et al. (1984), Maurin et al. (1986), Ajibade and Wright (1989), Benkhelil (1989), Guiraud et al. (1989), and Ngako et al. (2006), whereas those in Cameroon are from Ngako et al. (2006). (b) Satellite image map of the study area. (c) Geological map of Adamawa State showing the distribution of mineral deposits (extracted from the Nigerian Geological Survey Agency [NGSA], 2011). The locations of the mineral deposits are from the Ministry of Commerce, Industries and Solid Minerals Development (MCISMD, 2004).

The Nigerian basement complex preserved ~ 3000 Ma polycyclic tectonics (Obaje, 2009; Ominigbo, 2022; Dada et al., 2024), which reshaped the crust and generated structural pathways for hydrothermal mineralization (Kamaunji et al., 2022a). The Eastern Nigerian basement terrane (ENT), which is part of the Pan-African Central African Fold Belt, experiences multiphase tectonothermal events, shear zones, and granitic intrusions (Bute et al., 2022; Ferré et al., 1998, 2002; Halilu et al., 2025; Kamaunji et al., 2024, Fig. 1), conditions ideal for TIR-based mineral exploration (Mukhamedyarov, 2016; Zuo et al., 2023; Chao et al., 2024). Neotectonic activity from the Benue Trough and Cameroon Volcanic Line (Adebiyi et al., 2023; Apeh et al., 2024; Owono et al., 2024) enhances heat flow, pervasive faulting, and hydrothermal circulation, creating favourable conditions for barite mineralization (Dora et al., 2022; Wind et al., 2023; Samaoui et al., 2024).

The Mayo-Belwa (456 km2) and Jada-Ganye (3,500 km2) study areas within Nigeria's Eastern Basement Terrane (Fig. 2a–c) comprise Precambrian migmatite-gneiss complexes intruded by Pan-African Older granites (Kamaunji et al., 2022a). Situated in the northern Adamawa Massif, which extends into the Cameroon Volcanic Line (Figs. 1, 2a, c), these areas host barite deposits as basement-hosted veins (Mayo-Belwa peneplain) and cavity fillings (Jada highlands). Despite their economic potential, development is hindered by insufficient geospatial data and exploration frameworks to explore deeper deposit.

To bridge this gap, we present the Thermal Generalization Method (TGM), a novel algorithm that transforms thermal infrared data into 2D/3D thermodynamic models using a multichannel framework developed by Mukhamedyarov (1993, 2002, 2006, 2008, 2010a,b, 2011, 2012, 2016). TGM integrates symmetric input systems with algebra-geometric structures and advanced algorithms—generalization (G), automatic cell block identification (AICDS), vertical derivations (1VD, 2VD), and lithotemperature (LT) analysis—to effectively map high-purity barite deposits at depth (Mukhamedyarov, 2002–2016). The scientific and practical novelty of the TGM lies in its use of Earth's solid-surface thermal signals detected through electromagnetic radiation. By analysing both the spatial patterns and temporal dynamics (e.g., seasonal thermal variations and heat transfer mechanisms) of these surface temperature fields, TGM enables the effective characterization of subsurface material properties. (Mukhamedyarov, 2002–2016). This novel approach transforms passive thermal observations into active prospecting tools by integrating three key innovations: (1) multitemporal discrimination to isolate persistent thermal anomalies from transient surface effects, (2) heat transfer modelling to quantify conductive and convective processes linking surface signals to subsurface features, and (3) depth-resolved interpretation leveraging thermal inertia principles to profile material properties with depth (Mukhamedyarov, 1993, 2002–2016). TGM has proven effective across diverse applications, including hydrocarbon exploration in western Egypt (Tumanov and Cheban, 2013), identification of geoanthropogenic disturbances in Almaty, southeastern Kazakhstan (Mukhamedyarov, 2008), geotechnical characterization of construction sites on the Sakhalin Island, Russia (Bogatkin et al., 2011), and lithostructural mapping of kimberlite, basement hydrocarbons, and gold mineralization in eastern Nigeria (Mukhamedyarov, 2013).

This study applies high-resolution Landsat-7 ETM + thermal data, Shuttle Radar Topography Mission (SRTM) data, field observations, and TGM-based multichannel processing to map barite prospectivity in the Mayo-Belwa/Jada-Ganye area of the Eastern Nigerian Basement Terrane. By integrating thermal derivatives, lithostructural analysis, and water saturation thermodynamic modelling, thermally anomalous potential barite fields can be identified. The approach aims to characterize barite deposits; prioritize drill targets; and bridge remote sensing, geophysics, and mineral exploration through a novel, replicable strategy for assessing barite resources in complex basement terrains.

2. Geological background and barite mineralization

2.1. Eastern Nigerian terranes basement (ENT)

The Adamawa Massif, together with the Hawal Massif, forms Nigeria's Eastern Basement Terrane (ENT), which is bounded by the West Nigeria Terrane (WNT) and Northwestern Cameroon Terrane (Fig. 1). The Godé–Gormaya Shear Zone (GGSZ) and Raghane Shear Zone (RSZ) demarcate the eastern and western margins, respectively (Toteu et al., 2004; Dawaï et al., 2013). These Pan-African terranes constitute the Central Africa Fold Belt (CAFB), accreted from the Mayo-Kebbi, Adamawa-Yadé, and NW Cameroon domains (Toteu et al., 2004; Fig. 1). The WNT comprises Archaean tonalite–trondhjemite–granodiorite (TTG) suites, amphibolites, and gneisses (Ajibade et al., 1987), whereas the ENT features granites, diorites, metapelites, and migmatites (Onyeagocha and Ekwueme, 1990; Ferré and Caby, 2007; Kamaunji et al., 2021). Key contrasts include (1) ENT's tin mineralization versus the WNT's gold endowment (Woakes et al., 1987), and (2) ENT's Eburnean protoliths (linked to W Cameroon) versus WNT's Archaean dominance (Bruguier et al., 1994). The ENT is divided into the western ENT (W-ENT) and eastern ENT (E-ENT) by the Benue Trough/basin; an intracontinental rift formed during the Mesozoic as a result of the Atlantic Ocean spreading (Benkhelil, 1989) (Figs. 1, 2a). The E-ENT exhibits comparable tectonics, where ENE-WSW- and N-S-trending extensional fractures control the emplacement of fifty-three anorogenic alkaline complexes showing southwards age progression (Kamaunji et al., 2020, 2022b, 2023, 2024). The ENE fault system records major Pan-African transcurrent shearing (Maurin et al., 1986), with geophysical data showing a 20–30 km thick crust containing 6–10 km of mafic rocks (Shemang et al., 2001). These findings suggest that the Benue Trough overlies a deep Pan-African structure, interpreted as the Benue Trough Shear Zone (BTSZ) (Bute et al., 2020).

2.2. Adamawa Massif

The Adamawa Massif constitutes an elongated terrane within the Eastern Nigerian Terrane (ENT), bordering the southern Yola Arm of the Benue Trough and extending into southeastern Nigeria, where it is separated from the Oban Massif by the Lower Benue Trough (Fig. 2a). This massif is characterized by Pre-Cambrian migmatite-gneiss basement rocks intruded by Pan-African Older granites (Fig. 2a), preserving multiple tectono-metamorphic cycles (Ferré et al., 1998, 2002). The earliest deformation phase (D_1, ca. 638 Ma) involved *syn*-metamorphic low-angle thrusting during early Pan-African nappe tectonics, accompanied by the intrusion of fayalite monzonites and biotite granites (Dada and Respaut, 1989). This event was followed by D_2 (ca. 623–605 Ma), which was characterized by gently dipping foliations and N–S linear structures in two-mica granites and migmatites, reflecting crustal thickening (Dada et al., 1993). Subsequent D_3 deformation (ca. 587–577 Ma) comprised ductile dextral wrench faults that reworked earlier structures through refolding associated with crustal thinning (Ferré et al., 1996, 1998). The final phase (D4, ca. 550 Ma) featured N–S mylonites linked to cooling and exhumation along strike-slip faults (Ferré et al., 2002).

2.3. Barite mineralization and the local lithostructural framework

2.3.1. Barite mineralization in Nigeria

Barite mineralization in Nigeria occurs across both the Precambrian basement complexes and the NE–SW-trending Benue Trough (Fig. 2a), exhibiting diverse geological and structural controls that define its styles and associated mineral assemblages (Maurin and Benkhelil, 1990; Ebunu et al., 2021). Mineralization styles range from stratiform and nodular forms within the Abakaliki Basin to epigenetic, structurally controlled vein- and cavity-fill deposits that dominate the Benue Trough and adjoining basement terranes. In the Yola and Gongola Arms

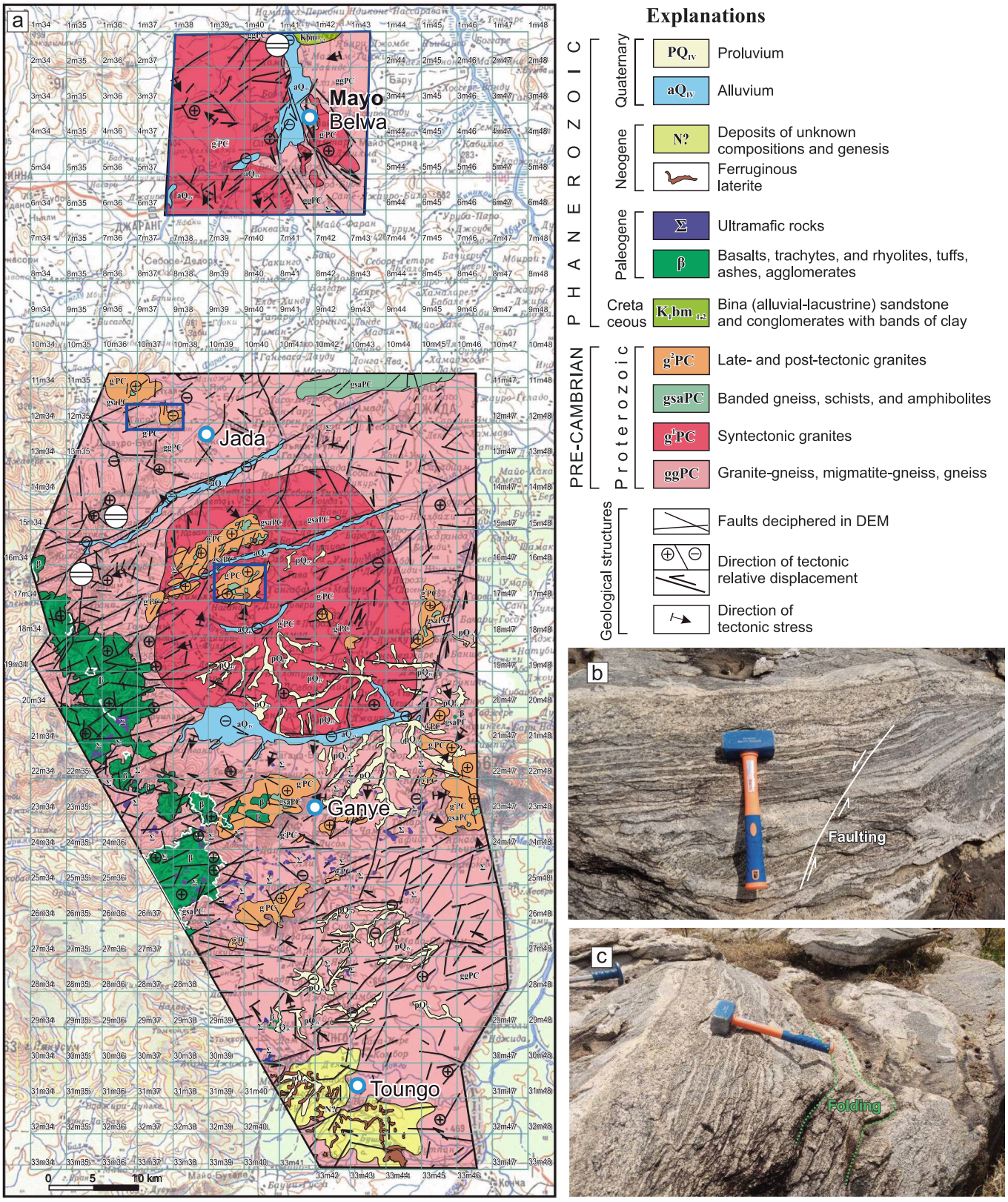

Fig. 3. (a) Geological map of the study area showing lineaments extracted from a digital elevation model (DEM); (b) Migmatitic gneiss outcrop displaying distinct banding and clear evidence of a reverse (thrust) fault. The banding reflects the complex metamorphic history of the gneiss, with the fault providing insight into the compressional tectonic processes affecting the region. (c) Migmatitic gneiss outcrop displaying clear folding of the rock layers, illustrating the deformation and bending of the gneissic bands. This provides insight into the tectonic forces responsible for folding and the region's complex structural history.

Fig. 4. (a) Syn-tectonic outcrop showing persistent NW–SE joints (278°) continuing across a N60°E-trending raised block, indicating pre-uplift formation or passive accommodation; (b) Late- to post-tectonic granite containing abundant MMEs with sharp, crenulated contacts and ellipsoidal shapes aligned with regional foliation, showing weakly foliated fabric without ductile overprinting; (c) NE–SW-oriented rhyolitic dikes and basaltic flows representing the final phase of Pan-African orogeny, overlain by Quaternary sediments; (d) Steep–walled barite mine pit in Precambrian migmatite–gneiss, showing quartz–barite veins cutting across foliation and partial oxidation along pit walls; (e) Irregular pit morphology following barite vein geometry in migmatite–gneiss, with residual lateritic soils overlying fresh bedrock exposures; (f) Massive reddish crystalline barite intergrown with quartz and minor sulfides in mine pit exposure; (g) NE–SW-oriented fracture-controlled barite veins in the Benue Trough, demonstrating tectonic–hydrothermal influence on mineralization; (h) NW–SE-trending barite vein system in the Benue Trough, showing structural control of.

(Adamawa: 0.332 Mt; Gombe: 0.353 Mt), basement-hosted mineralization occurs as high-grade vein-type deposits (0.3–4.3 m wide) in granitic and migmatitic rocks, with specific gravities of 4.0–5.3 (NGSA, 2011; Ebunu et al., 2021). In contrast, sedimentary-hosted deposits in Benue (0.308 Mt), Cross River (8.6 Mt), Nasarawa (3.2 Mt), and Taraba (9.0 Mt) show greater dimensional variability (cm to 5.8 m wide, locally up to 150 m in Benue) and lower purity (SG 3.5–4.4) due to abundant gangue minerals (Labe et al., 2018; NGSA, 2011).

In the Abakaliki Basin (Lower Benue), barite mineralization is expressed as stratabound concordant beds, discordant veins (10 cm–8 m wide, average ~ 1 m), and disseminated nodules, hosted within arkosic sandstones, fractured shales, and intrusive bodies of the Asu River Group (Ene & Okogbue, 2012, 2016). Structural control by NW–SE and N–S fractures is well established, with mineralization linked either to magmatic-hydrothermal activity associated with intrusives and brine ponds (Offodile, 1989), or to expulsion of basinal brines during Cenomanian tectonism (Akande et al., 1989; Uma, 1998). The paragenesis typically includes barite with Pb–Zn sulfides (galena, sphalerite), minor copper sulfides, fluorite, and calcite.

Similarly, deposits in Ishiagu, Enyigba–Ameki–Ameri, Wanikande–Wanakom, and Gabu–Oshina (Andrew-Oha et al., 2017) confirm fracture control by Santonian faulting. The mineralogical variations reflect host lithologies and fluid composition: Pb–Zn–dominated sulfides at Ishiagu and Enyigba; mixed Pb–Zn–barite with dioritic to nepheline syenite intrusives at Wanikande–Wanakom; and barite-dominant mineralization in Eze-Aku sandstones and doleritic sills at

Gabu–Oshina (Andrew-Oha et al., 2017). This spatial progression marks a transition from Pb–Zn-rich to barite-rich systems northeastward along the basin.

Barite from multiple Nigerian deposits shows variable quality and gangue (Abraham et al., 2021). Veins and cavity fillings in mudstones, shales, limestones, sandstones, and siltstones range from a few cm to ~ 6 m thick. Ores are dominated by $BaSO_4$, with quartz, hematite, celestite, and calcite. SG ranges from 2.9 to 4.3; higher-grade ores (Benue, Taraba) meet API standards, lower-grade (Plateau, Nasarawa) require beneficiation. In the Middle Benue (Arufu, Akwana, Azara), barite is intimately associated with Pb–Zn–fluorite veins hosted by Albian–Turonian sediments (Akande et al., 1989). At Azara, barite is particularly abundant, whereas Arufu and Akwana display fluorite–barite–calcite–quartz assemblages. Fluid inclusion studies indicate moderate-temperature (95–200 °C), saline brines (14–24 wt% NaCl eq.), with isotopic data supporting derivation from basinal fluids modified by shales, carbonates, and evaporites. Sulfur isotopes reveal thermochemical sulfate reduction of Cretaceous evaporites, aided by methane-rich fluids, while Sr and Pb isotopes suggest input from the Precambrian basement. These features are consistent with a basinal brine expulsion model for hydrothermal fluid flow.

In Nasarawa and Taraba States (e.g., Azara, Keana, Wuse, Ribi, Suani), barite occurs mainly as cavity-filling vein systems localized within sandstones and basement rocks, forming tabular to lensoid bodies (Otoijamun et al., 2021; Ottan et al., 2022). Veins vary from millimetres to > 5 m thick, with lateral continuity of up to 1 km and depths exceeding 30 m. The ores, typically intergrown with hematite, quartz, siderite, and sulfides (galena, sphalerite), display SG values of 3.9–4.5, with many meeting API standards for drilling muds. However, high silica, carbonate, and iron oxide contents in some veins necessitate beneficiation. Artisanal mining dominates these areas, leading to poor recovery and environmental risks from Pb contamination (Ottan et al., 2022).

Barite in the Mid-Nigerian Benue Trough is structurally controlled, correlating with lineament density, ferric alteration, and high K/Th ratios (Gajere et al., 2024). Deposits occur in faulted Cretaceous sequences as vein-type hydrothermal mineralization, associated with iron oxides and silicate gangue. High-potential zones cover ~ 19 % of the area, highlighting the importance of structural and geospatial controls in exploration. Elsewhere in the Benue Trough and adjoining basement terrains, mineralization occurs as epigenetic hydrothermal veins and cavity fills, commonly within faulted and brecciated sandstones or fractured basement rocks. Examples include the Faya deposit in Plateau State, where barite forms veins and pore fillings (100–150 m long, 1.5–2.5 m wide) with quartz, biotite, pyrite, magnetite, and secondary siderite and goethite (Samaila et al., 2025). Across the Benue Valley, paragenetic assemblages are dominated by barite, galena, sphalerite, fluorite, quartz, calcite, siderite, and iron oxides, with systematic thermal and chemical gradients reflecting district-scale fluid evolution (Ogundipe, 2017; Sunday et al., 2020).

Overall, Nigerian barite mineralization is best classified as dominantly epigenetic vein- and cavity-fill deposits, locally accompanied by stratiform and nodular bodies in the Abakaliki Basin. Mineralization styles transition from high-grade, small-volume basement-hosted veins (Adamawa, Gombe) to more extensive but variable-quality sedimentary-hosted systems (Cross River, Nasarawa, Taraba, Benue). Associated gangue and accessory minerals include quartz, calcite, dolomite, siderite, feldspar, fluorite, galena, sphalerite, chalcopyrite, pyrite, hematite, and magnetite, reflecting strong structural and hydrothermal controls. Reserve distribution also varies: Cross River and Taraba host the largest deposits (~8.6–9.0 Mt), while basement terranes (Gombe, Adamawa) yield smaller but higher-grade resources. Nationwide, reserves exceed 22 Mt, underscoring Nigeria's significance as a barite province (NGSA, 2011; MMSD, 2018; Afolayan et al., 2021; Gajere et al., 2024).

2.3.2. Local lithostructural framework

The study area, covering Mayo-Belwa (456 km^2) and Jada-Ganye-Toungo (3,500 km^2) (Fig. 2b), forms the northern Adamawa Massif in the ENT (Fig. 2a) and the southern basement terranes of Adamawa Province (Fig. 2c). The area is underlain by migmatite-gneisses, syntectonic, and late- to post-tectonic granites (Figs. 2c, 3a), with a dominant NNE–SSW lineament network and prominent NNW–SSE-oriented stresses, indicating significant compressional or shear tectonics that reactivated faults and/or formed new fractures (Barton and Angelier, 2020). The subordinate NNE–SSW stress direction suggests a secondary, localized deformation phase (Fig. 3a).

The migmatite-gneisses display distinct melanocratic-leucocratic banding (Figs. 3b, c), recording multiple Precambrian metamorphic and deformational phases (Dada, 2008). The structures include (1) steep fault zones with offset markers indicating brittle deformation (Fig. 3b) and (2) tight asymmetric folds (~60° interlimb angle) with axial cleavage, showing thickened hinges and thinned limbs from flexural slip (Fig. 3c). These features document progressive deformation from early ductile folding (D_1) to brittle faulting (D_2) during exhumation (Augier et al., 2013).

The migmatite gneisses are intruded by syntectonic granites forming large subcircular outcrops with persistent NW–SE joints (278°; Fig. 4a) and late- to post-tectonic varieties with irregular shapes, abundant MMEs (foliation-aligned ellipsoids; Fig. 4b), and weak fabrics indicating late-stage emplacement. The Pan-African climax involved faulting, hydrothermal activity, and mineralization (McCurry, 1971), followed by NE–SW rhyolitic dikes and basaltic flows (Fig. 4c). Quaternary denudation reshaped these terrains along structural trends.

2.3.3. Barite mineralization in the area

Barite mineralization in the area is structurally controlled, occurring mainly as vein- and cavity-fill deposits along fault and fracture zones. The barite mine pits in the basement gneisses display steep, irregular geometries mirroring vein orientations in Precambrian migmatite gneiss (Figs. 4d, e). Quartz-barite veins (0.5–3 m thick) cut across basement foliation and weathered pit walls show oxidized host rocks beneath lateritic soils (Figs. 4d, e). The barite occurs as massive reddish crystalline masses, commonly intergrown with quartz and minor sulfides such as galena and sphalerite (Fig. 4f). These features are consistent with basement-hosted vein-type barite deposits reported in elsewhere in Adamawa and Gombe, where high-grade veins (0.3–4.3 m wide; SG 4.0–5.3) occur within granitic and migmatitic rocks (NGSA, 2011; Ebunu et al., 2021). They are also comparable to vein- and cavity-fill deposits in the Abakaliki Basin and Taraba, which also show structural and hydrothermal controls (Labe et al., 2018; Abraham et al., 2021). These observations confirm that the mineralization style in the area is dominantly vein-type, with hydrothermal fluids exploiting structural weaknesses in the basement rocks. Artisanal works (10–50 m long, 5–15 m deep) demonstrate manual extraction along vein systems..

Benue Trough barite deposits form NE–SW/NW-SE-trending fracture-controlled veins (Figs. 4g, h), reflecting tectonic–hydrothermal origins. In the Benue Trough, along the basement-sedimentary interface in Mayo-Belwa, barite occurs as NE–SW and NW–SE-trending veins typically hosted in sandstones, shales, and siltstones, analogous to deposits in Nasarawa and Taraba where veins are associated with gangue minerals such as quartz, calcite, siderite, and fluorite (NGSA, 2011; Gajere et al., 2024). The combination of structural control, host lithology, and mineral assemblages indicates that these deposits represent epigenetic vein-type barite mineralization, formed through tectono-hydrothermal processes and commonly associated with gangue minerals such as quartz, calcite, siderite, and fluorite, analogous to well-studied hydrothermal vein systems in the Benue Trough and basement terranes, including Adamawa, Gombe, Nasarawa, Taraba, and the Abakaliki Basin (NGSA, 2011; Labe et al., 2018; Abraham et al., 2021; Ebunu et al., 2021; Gajere et al., 2024).

Although the Nigerian barite deposits are predominantly epigenetic

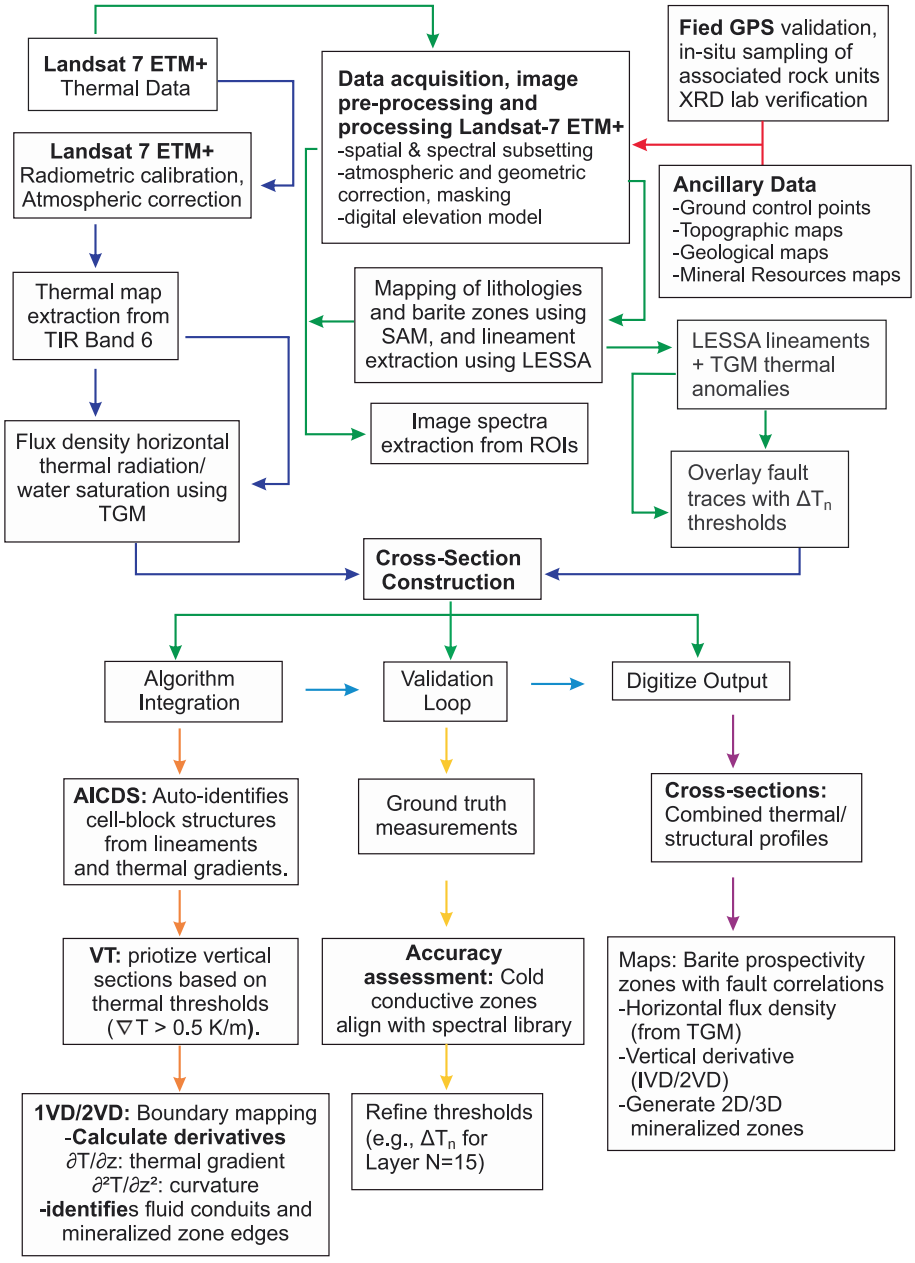

Fig. 5. Workflow diagram of the integrated Landsat 7 ETM* thermal data processing and barite exploration methodology. The schematic outlines key steps from data acquisition (radiometric calibration, atmospheric correction) to advanced processing via the thermal generalization method (TGM) and automated identification of cell-block structures (AICDS) algorithm. The critical components include (1) thermal map extraction from TIR Band 6; (2) flux density and water saturation calculations; (3) lineament extraction (LESSA) and spectral mapping (SAM); (4) derivative analysis (IVD/2VD) for fluid conduit identification; and (5) 3D prospectivity modelling with field validation (XRD, GPS). Threshold refinement (e.g., ΔT_n for Layer N = 15) and vertical section prioritization ($\nabla T > 0.5$ K/m) guide target selection.

vein- and cavity-fill systems hosted in basement gneisses and Cretaceous sediments, their mineralogical and geochemical characteristics show notable parallels with hydrothermal barite formation in rift-related carbonate sequences, such as those reported along the Dead Sea Transform Fault (Dill et al., 2012a). In both settings, barite precipitated from hydrothermal fluids, forming mineral assemblages that include Ba-rich sulfates, carbonates, and silicates, with crystal morphology influenced by fluid chemistry, cation availability, and minor organic or detrital phases. While the Nigerian deposits are structurally controlled, fracture-hosted veins, the Dead Sea system illustrates barite formation under low-temperature hydrothermal conditions in transitional subaqueous-to-subaerial environments, highlighting that similar hydrothermal processes can operate across diverse tectonic and depositional contexts. Similarly, the Miesbrunn pegmatite–aplite swarm (Dill et al., 2012b) in Germany exhibits structural and hydrothermal analogies with the Nigerian barite deposits. In both systems, mineralization is localized along reactivated fractures or shear zones, controlled by episodic hydrothermal fluid flow, and displays temperature- and redox-dependent zoning. Near-surface alteration modifies primary mineral assemblages, whether Fe phosphates in MPAS or oxidized sulfides and intergrown quartz in Nigerian barite, emphasizing the key role of tectono-hydrothermal processes in ore localization.

3. Methodology

3.1. Landsat data acquisition and processing

This study utilized four cloud-free Landsat-7 ETM + images (Supplementary Fig. 1) processed through atmospheric correction (QUAC/MODTRAN), emissivity normalization (NDVI threshold method), and topographic correction (SCS + C). SRTM-derived terrain data and lineament analysis (LESSA) were integrated with thermal anomalies (validated RMSE: ±1.2 °C) to map barite prospects. Thermal anomalies were identified using Landsat-7 Band 6 data (10.4–12.5 μm) calibrated following USGS (2019a) protocols. Potential barite fields were detected based on characteristic thermal signatures (~3 μm) and validated through field measurements (R^2 = 0.89) and ASTER LST comparisons (RMSE ± 1.2 °C). Detailed methodological descriptions, including atmospheric correction and spectral enhancement procedures, Shuttle Radar Topography Mission (SRTM) DEM development are provided in Supplementary Material 1, and the methodological workflow is illustrated in Fig. 5.

3.2. Thermal generalization method (TGM)

The thermal generalization method (TGM) is an advanced analytical framework that processes thermal infrared data to create three-dimensional thermodynamic models of Earth's surface radiation, enabling the detection of subtle temperature variations and the characterization of subsurface lithology and structural features (Mukhamedyarov, 1993, 2002–2016). This method introduces two innovations: first, it redefines solar energy's role in heat transfer by treating surface-derived thermal energy as a dominant diagnostic signal (four orders of magnitude stronger than deep thermal fluxes), transforming solar radiation into a powerful tool for mineral system analysis; second, it pioneers a systematic approach to differentiate heat-transfer mechanisms (convection, conduction, and hybrid processes) through quantitative analysis of thermal radiation patterns and their seasonal variations, overcoming traditional limitations that dismiss the influence of solar energy as noise in crustal heat studies (Mukhamedyarov, 1993, 2002–2016).

The thermal generalization method (TGM) operationally integrates remote sensing and subsurface geophysics through a multichannel algorithmic framework. Its core computational modules—Generalization Algorithm (G), Automatic Identification of Cell-Block Structure (AICDS), and Litho-Temperature (LT)—transform 2D thermal infrared imagery into 3D models via algebra-geometric transformations (Mukhamedyarov, 2002–2016). By synthesizing thermal, hydraulic, and structural data, TGM enables high-resolution lithospheric imaging that detects anomalous mass–energy exchange across geological strata. The resulting layered thermal models show consistent alignment with multispectral surface imagery, adhere to nonequilibrium dissipative structure principles, and correlate with independent geophysical datasets (Mukhamedyarov, 1993, 2002–2016).

Compared with traditional techniques such as borehole temperature measurements—which are spatially constrained and impractical for regional-scale analysis—TGM offers a cost-effective, scalable solution with continuous data coverage. Its ability to resolve subsurface fluid pathways and fracture zones with precision comparable to that of seismic methods (and in some cases superior for detecting vertical fluid dynamics) underscores its transformative potential for mineral exploration and Earth system science (Mukhamedyarov, 1993, 2002–2016). These algorithms are detailed below:

3.2.1. Generalization algorithm (G)

This algorithm enhances parametric sensitivity (not spatial resolution) through frequency filtering and deeper horizontal penetration, enabling continuous depth sensing of thermal anomalies. It employs a 3D pyramid weighting function to quantify crustal thermal radiation contributions to surface elements. The type of generalization is determined by the relation (Mukhamedyarov, 2002–2016).

$$(\sigma_{x,y}) = \frac{\left[\sum_i^{N_x}\sum_j^{N_y}(K_{ij}\bullet E_{ij})^{\alpha}\right]^{1/\alpha-\beta}}{\sum_i^{N_x}\sum_j^{N_y}(K_{ij}\bullet E_{ij})^{\beta}}$$

In the particular case where $\beta = \alpha - 1$

$$(\sigma_{x,y}) = \frac{\sum_i^{N_x}\sum_j^{N_y}(K_{ij}\bullet E_{ij})^{\alpha}}{\sum_i^{N_x}\sum_j^{N_y}(K_{ij}\bullet E_{ij})^{\alpha-1}}$$

For $\alpha = 0$, the equation represents the harmonic mean:

$$(\sigma_{x,y}) = \frac{N_x N_y}{\sum_{j=1}^{N_y}\sum_{i=1}^{N_x}(K_{ij}\bullet E_{ij})^{-1}}$$

For $\alpha = 1$, the equation represents the arithmetic mean:

$$\varphi(\varepsilon_{x,y}) = \frac{\sum_{j=1}^{N_y}\sum_{i=i}^{N_x}(K_{ij}\bullet E_{ij})}{N_x N_y}$$

The signal received by the *i*-th receiver is given by:

$$E_{ij} = A \bullet S_{\lambda MARCi} \bullet \int_{\lambda il}^{\lambda i2} \varepsilon_{\lambda T} \bullet C_i \bullet \lambda^{-5} \bullet (\exp(c_2/(\lambda\cdot T)) - 1)^{-1}\cdot\alpha_{\lambda i} d\lambda,$$

where A = a coefficient characterizing the optical system; *SλMAkCi* = maximum spectral sensitivity; $a\lambda$ = relative characteristic of the receiver; $b_{\lambda T}$ = the spectral distribution of the radiation energy density: $b_{\lambda T} = \varepsilon_{\lambda T}\cdot C1\cdot\lambda_{-5}(\exp(C_2/(\lambda\cdot T)) - 1)^{-1}$; $\varepsilon_{\lambda T}$ = the emissivity of the object; $C_1 = 3.7413\cdot 10{-}12$ W · cm^2: A constant; $C_2 = 1.4388$ cm · K: A constant; λ = emission wavelength in microns (μm); T = temperature.

In geophysical settings, α and β are fractional, thus permitting the selection of values representing the depth of penetration h_i at each generalization stage N, both in spatial and spectral resolution (Mukhamedyarov, 1993), as well as type of generalization, for instance, the harmonic mean at $\beta = \alpha$-1, $\alpha = 0$, to sum up the different layers in terms of thermal conductivity. Hence, the penetration depth h_N at layer level N on the ground surface can be calculated via the following equation (Mukhamedyarov, 2002, 2013):

$$H_N = \frac{H^2}{H_T + H}\left(\frac{N\delta}{2} + \frac{N^2\delta^2}{4}\right);$$

where N = number of horizontal layers (generalization stages); h_T = estimated distance from the object of study to the Earth's surface; H = distance from the sensor imaging equipment to the Earth's surface; and δ = the angular spatial resolution (in radians) of imaging equipment follows the resolvability-limit relationship: $\delta\ell\Delta T_p = constant$, where δ = spatial resolution element, ΔT_p = radiation temperature noise (characterizing thermal imaging parameters), and ℓ = constant (2.5–2.72). This reflects a trade-off between resolution and temperature sensitivity. Generalization levels are defined by integer series: 1, 2, 3,… (Mukhamedyarov, 2002, 2013). The zero layer is a panchromatic image based on visible-range reflectance, whereas the first generalization layer is a thermal image (7.5–13.5 μm) or derived from equations (1) and (5) for $N = 1$. Its penetration depth (h_1) equals half the pixel size: h $h1 = \delta x,y/2$. Aerospace video thermal imaging is tied to the radiometric temperature: $T_{PB} = \sqrt[4]{\varepsilon}\cdot T_{TB}$, where ε = the emissivity of the target object; T_{TB} = the thermodynamic temperature; and $\delta^2 \times$ (1, 4, 9, 16, 25, etc.) = the area corresponding to each degree of generalization (Mukhamedyarov, 2002, 2013).

The land surface emissivity (ε) ranges from 0.8 to 0.97, and the land surface is heated during the day and cooled at night. The geothermal gradient h $\Gamma(T) = -\frac{\partial T}{\partial h} = -\frac{q\varepsilon}{\lambda T}$ quantifies the temperature change with depth (h), revealing nonuniform thermal fields. The heat flow density ($q\Sigma$) combines conduction (q_k), convection ($q\lambda T$), and radiation (q_n). The second temperature derivative with depth is related to temporal

changes and thermal diffusivity, identifying minor inhomogeneities and medium thermal capacity. The horizontal gradient $G(T) = \frac{\partial T}{\partial h\left(\frac{\partial T}{\partial L}\right)}$ maps the temperature variation along the horizontal axis L, where T(G) represents the temperature along the horizontal axis L, T_Γ = the thermodynamic temperature on the horizontal line L, and $\partial T/\partial h$ = the rate of temperature change with time (Mukhamedyarov, 2002–2010, 2013). The generalization algorithm (G) was validated through theoretical analysis of its mathematical framework, empirical testing against ground measurements, and field benchmarking (Mukhamedyarov, 2002, 2010–2016), confirming its reliability for thermal analysis applications.

3.2.2. The automatic identification of the Cellblock structure (AICDS)

The AICDS is designed to automatically detect and visualize cell-block structures, particularly in geological or geophysical contexts. It processes thermal data to identify lineaments (linear features) in vertical and subhorizontal sections, assessing their severity, contrast, and validity. The algorithm begins by calculating the gradient of temperature or other geophysical properties (Mukhamedyarov, 1993, 2002, 2013): $\nabla T = \left(\frac{\partial T}{\partial x}, \frac{\partial T}{\partial y}, \frac{\partial T}{\partial z}\right)$,

where T represents the temperature or other geophysical property at coordinates (x, y, z). Regions with significant gradient changes are identified as potential cell-block boundaries. A weighting function is then applied to emphasize significant features: $W(x, y, z) = f(\nabla T, \delta)$, where δ is the spatial resolution. The algorithm classifies the severity and contrast of lineaments by thresholding:

$$Severity = \begin{cases} High if |\nabla T| > \tau_1 \\ Mediumif \tau_2 < |\nabla T| \le \tau_1 \\ Low if |\nabla T| \le \tau_2 \end{cases}$$

where τ_1 and τ_2 are predefined thresholds. The validity of the detected features is assessed by comparing them with known geological structures or ground truth data. The final output is a detailed visualization of the cell-block structure, highlighting lineaments and their characteristics. This algorithm provides a robust tool for analysing subsurface structures, optimizing exploration efforts, and supporting applications in geological exploration, resource management, and environmental monitoring (Mukhamedyarov, 1993, 2002, 2013). The AICDS algorithm interprets thermal radiation data to identify features such as high water saturation. The dark bands in the image, which are linked to lower temperatures or higher thermal inertia, indicate areas with high water content due to the high heat capacity of the water. The algorithm uses thresholding to correlate these dark bands with high water saturation, classifying them on the basis of (x, y) coordinates.

$$\begin{cases} HighWaterSaturation, if T(x,y) < T_{threshold} and W(x,y) > W_{threshold} \\ LowWaterSaturation, otherwise \end{cases}$$

where T(x,y) represents the thermal radiation field at coordinates (x,y), W(x,y) represents the water saturation level at (x,y), and $T_{threshold}$ and $W_{threshold}$ represent predefined thresholds for temperature and water saturation, respectively. The algorithm validates interpretations by integrating water saturation models for accuracy. The final output visualizes dark bands as cold thermal radiation fields with high water saturation and bright bands as warmer, drier regions. This enables the automatic detection and visualization of high-water saturation areas, offering valuable insights for geological studies. The detected features were statistically compared with ground truth data. Thermal radiation interpretation (e.g., high-water saturation zones) was verified via water saturation models, whereas output visualizations of structures and saturation were cross-checked, confirming its reliability for geological/environmental applications monitoring (Mukhamedyarov, 2013).

3.2.3. The algorithm GS (Geological Structure)

The geological structure (GS) algorithm identifies and visualizes anomalies in geological data, such as thermal, seismic, or electromagnetic measurements. It generates 2D/3D maps with colour gradients to highlight areas of interest, such as fault zones related to barite mineralization. The algorithm detects anomalies via the equation A(x,y,z) = |D (x,y,z) − μD|, where D(x,y,z) represents the geophysical data, μD represents the mean value, and A(x,y,z) represents the anomaly magnitude. It then enhances the contrast between anomalies and the background by applying the following equation: $C(x,y,x) = A(x,y,z)/\sigma D$, where σD is the standard deviation of the data and $C(x,y,z)$ represents the contrast-enhanced anomaly. The algorithm visualizes results by mapping C(x,y,z) onto a 2D or 3D grid, using colour gradients to represent anomaly intensity. This enables clear identification of geological structures and anomalies, making it a valuable tool for exploration and analysis. The outputs were compared with known geological structures and ground truth data (Mukhamedyarov, 1993, 2002–2013).

3.2.4. Algorithm LT (Litho-temperature)

The Algorithm LT (litho-temperature) is designed to map the density of thermal radiation and relative water saturation on horizontal slices at specified depth intervals. The algorithm begins by extracting horizontal slices of thermal radiation T(x,y,z)$T(x,y,z)$ and water saturation W(x,y,z)$W(x,y,z)$ data at specified depths. The thermal radiation density is calculated via equations. $Td(x, y, z) = \partial T(x, y, z)/\partial z$, where $T(x,y,z)$ represents the thermal radiation at coordinates (x,y,z) and Td(x,y,z) represents *the* thermal radiation density at depth z. The relative water saturation is determined by $W(x,y,z) = \frac{Vw(x,y,z)}{Vp(x,y,z)}$, where Vw(x,y,z) = the volume of water at (x,y,z); Vp(x,y,z) = the pore volume at (x,y,z); and W (x,y,z) = the relative water saturation. For each depth interval z*i*, the algorithm generates 2D maps of Td(x,y, zi) and W(x,y, zi), providing a detailed visualization of the thermal radiation density and water saturation across horizontal slices. This approach is particularly useful for analysing subsurface thermal properties (Mukhamedyarov, 1993, 2002–2013).

3.2.5. Algorithm VT (Vertical temperature)

The Algorithm VT (vertical temperature) determines the order of construction of the vertical sections of the geothermal field and the relative water saturation. The algorithm constructs vertical sections of the geothermal field and water saturation, prioritizing sections on the basis of data significance or anomaly intensity. The geothermal field vertical gradient is calculated via: $GT(x,y,z) = \partial T(x,y,z)/\partial z$, where T(x, y,z) = temperature at coordinates (x,y,z) and GT(x,y,z) = the vertical temperature gradient. Similarly, the water saturation vertical gradient is determined by $GW(x,y,z) = \partial W(x,y,z)/\partial z$, where W(x,y,z) represents the relative water saturation at (x,y,z) and GW(x,y,z) represents the vertical water saturation gradient. The algorithm ranks vertical sections on the basis of anomaly intensity or gradient magnitude via the following significance score: $S_i = \int_{z_{min}}^{Z_{max}} |G_T(x, y, z)| + |G_W(x, y, z)| dz$, where Si = the significance score for the i*i*-th vertical section, and sections with higher Si are prioritized for construction and visualization. This approach ensures that the most significant vertical sections are highlighted, providing valuable insights into the geothermal field and water saturation distribution (Mukhamedyarov, 1993, 2002–2013).

3.2.6. Algorithm 1VD (First vertical Derivation)

Algorithm 1VD (1 Vertical Derivatives) is designed to visualize the results of the first derivative of the vertical sections of the geothermal field and the field of water saturation. The algorithm computes the first derivative of the geothermal field and water saturation along the vertical axis via the following equations: first derivative of the geothermal field: $G\frac{(1)}{T}(x, y, z) = \partial T(x, y, z)/\partial z$, where $\partial T(x, y, z)$ = temperature at coordinates (x, y, z); $G\frac{(1)}{T}$ (x, y, z) = first derivative of the geothermal

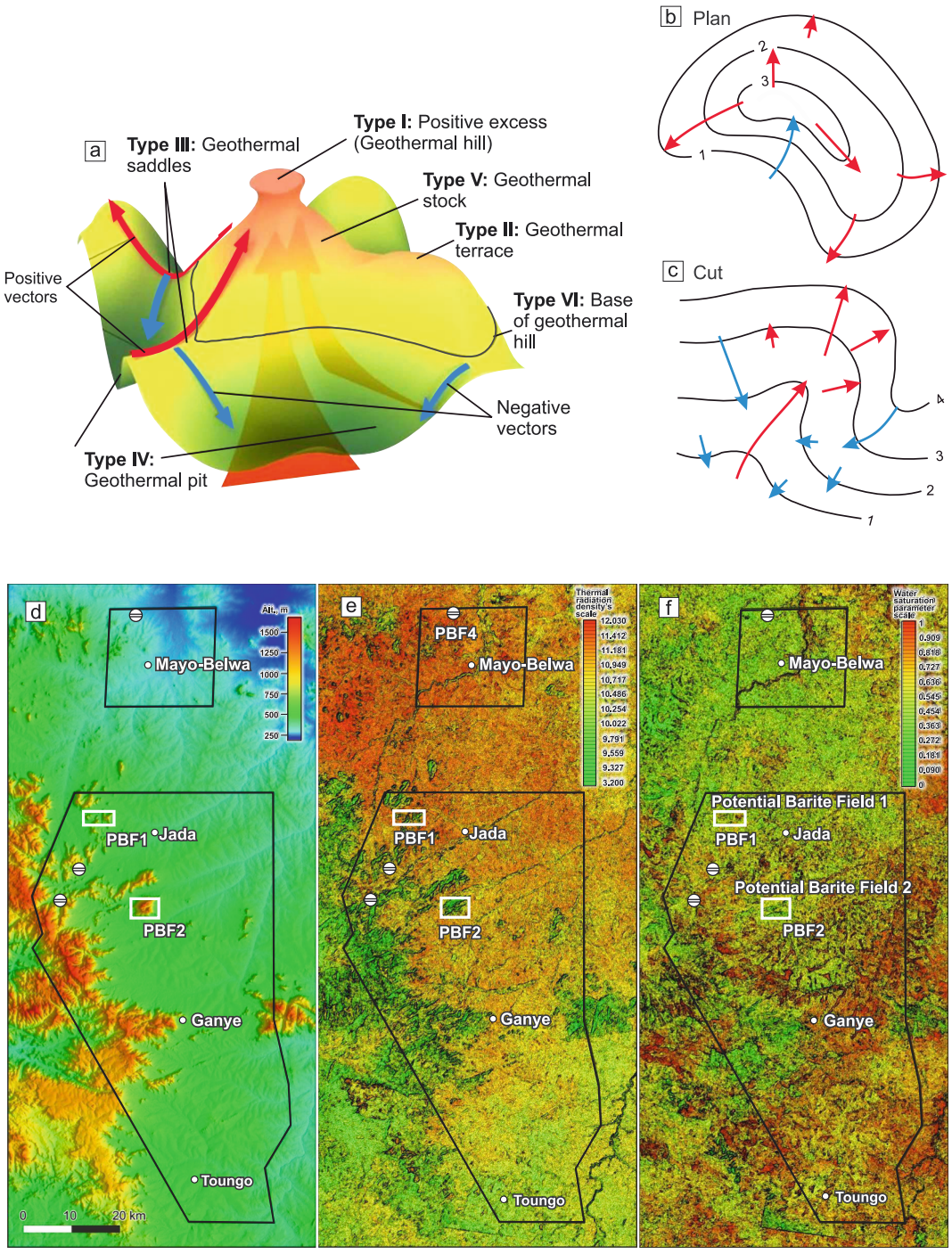

Fig. 6. (a) Geometric heat cell classification (Tumanov, 2007) showing six geothermal features: hills (I), terraces (II), pits (IV), stocks (V), and hill bases (VI). The vectors indicate the thermal flux direction (red = positive/rising, blue = negative/subsiding). This formal taxonomy distinguishes structural features in rising thermal current zones (hills, stocks, terraces) from those in negative flux regions (pits, linear sinks) at 1:100,000–200,000 mapping scales. Contour curvature vector analysis of numerical model parameters: (b) plan view and (c) vertical cut showing curvature vectors: red arrows indicate positive curvature (directed from high to low values), and blue arrows indicate negative curvature (low to high values). Vectors are plotted at points of maximum contour curvature to identify critical geometric features in the digital model. This formal analysis procedure tracks curvature extrema across both horizontal and vertical sections to characterize 3D morphological patterns. Comparison of (d) digital elevation model (DEM) and (e) flux density of thermal radiation and (f) flux density of relative water saturation at a depth of 60 m. Comparison of surface thermal radiation, water saturation, and elevation at 60 m depth: (d) digital elevation model (DEM) and (e) thermal radiation density show an inverse correlation between altitude and temperature, with higher elevations generally cooler. (f) Water saturation is correlated with elevation, with higher areas showing greater saturation, particularly in the upper pen plain. The eastern and southeastern regions are more arid. Local water saturation anomalies are analysed in subsequent prospecting sections.

Table 1
Quantitative comparison of summer and winter thermal–hydrological parameters in the study area.

Season	Mean Thermal Radiation Density (W m^{-2})	Standard Deviation (W m^{-2})	Mean Water Saturation Parameter (dimensionless)	Correlation r (T(rad) vs WSP)
Dry (April–May)	10.42	1.12	0.46	–0.72
Wet (Aug–Sep)	8.67	0.84	0.63	–0.72

field along the vertical axis. First derivative of the water saturation field: G $\frac{(1)}{W}$ (x, y, z) = ∂W(*x, y, z*)/∂z, where ∂W(x,y,z) represents the water saturation at coordinates (x,y,z); G $\frac{(1)}{W}$(x,y,z) represents the first derivative of the water saturation field along the vertical axis. The algorithm then generates vertical sections of G $\frac{(1)}{T}$(x,y,z) and G $\frac{(1)}{W}$ (x,y,z) for visualization, providing insights into the rates of change in temperature and water saturation with depth (Mukhamedyarov, 1993, 2002–2013).

3.2.7. Algorithm 2VD (2nd Vertical Derivation).

Algorithm 2VD (2 Vertical derivation) visualizes the results of the - second derivative of the vertical sections of the geothermal field and the field of water saturation. The algorithm computes the second derivative of the geothermal field and water saturation along the vertical axis via the following equations: Second derivative of the geothermal field: G $\frac{(2)}{T}$ *(x, y, z)* = ∂^2T(*x, y, z*)/∂z^2, where G $\frac{(2)}{T}$(x, y, z) = second derivative of the geothermal field along the vertical axis. Second derivative of the water saturation field: G $\frac{(2)}{W}$ *(x, y, z)* = ∂^2*W*(*x, y, z*)/∂z^2, where G ((2))/*W* (x,y,z) represents the second derivative of the water saturation field along the vertical axis (Mukhamedyarov, 1993, 2002–2013).

4. Results Interpretation: Thermal Imaging Data

4.1. Distribution and characteristics of geothermal structures

Characterizing the Earth's thermal radiation field is challenging because of the lack of standardized terminology for thermal processes. To address this, frameworks from geothermal science, hydrogeology and tectonics are integrated, although their terms are only approximate analogs (Prakash, 2000). The Tumanov (2007) geothermal model introduces standardized terms, including heat cell configurations, thermal vector patterns, and hierarchical block–cell relationships, which account for depth-dependent thermal variations and conductive–convective interactions. This model helps identify localized anomalies, large-scale structures, and transitional features, such as geothermal hills, negative anomalies, homogeneous geothermal stocks, geothermal terraces, linear currents, and transitional saddles (Fig. 6a; Tumanov, 2007). This technique aids in mapping subsurface heat distribution, supporting geothermal exploration by distinguishing heat discharge/absorption zones and identifying uniform thermal regions. For barite prospectivity mapping, we integrate Tumanov (2007) geothermal cell classification with Mukhamedyarov's multichannel TGM (1993, 2002–2016).

4.2. Key elements in the numerical models for cross-section construction

This procedure analyses digital and graphical model parameters, which are traditionally performed manually, to construct geological cross-sections. It involves tracking vectors of positive or negative curvature along contour lines in vertical and planned cuts. Positive vectors point from high to low values, and negative vectors extend from low to high values (Figs. 6b, c). The graphic documents for interpretation include vertical sections, horizontal slices from digital models, and surface parameters from satellite imagery. The process begins with Algorithm VT (vertical temperature), which prioritizes vertical sections on the basis of thermal gradient thresholds (e.g., $\nabla T > 0.5$ K/m) and anomaly intensity. The thermal flow vectors are analysed on the initial sections of the thermal radiation field and transferred to the first and second derivative sections via Algorithm 1VD/2VD (Mukhamedyarov, 2013). The first derivative shows the overall thermal field structure, whereas the second derivative provides a more geologically consistent view by representing acceleration dynamics in thermal processes (Mukhamedyarov, 2013). These analytical results are cross-referenced with multiple datasets, including automated cell-block structures from Algorithm AICDS, geological and geophysical data, drilling results, and geophysical surveys. The workflow integrates Algorithm LT (litho-temperature) to map the thermal radiation density and water saturation at specific depths. Geothermal anomalies are classified in relation to vertical hydrogeological zoning, block-fault structures, and lithological complexes, with attention to vector adjustment zones distinguishing conductive, convective, and mixed heat-mass transfer mechanisms (Mukhamedyarov, 2013, 2016).

For the 3D relative water saturation model, the process involves the following steps: (1) Vector selection, (2) second-derivative plotting and interpretation, and (3) comparison with automated cell-block structure results. This multialgorithm approach, validated with field measurements and georeferenced Google Earth imagery, allows precise cross-section reconstruction while resolving subsurface stress regimes and mineralization controls (Mukhamedyarov, 2013, 2016). The integration of these methods often reveals fault tectonic elements in the second derivative of thermal radiation sections, with better layering resolution than in the original thermal radiation field. The methodology combines manual vector analysis with algorithmic processing to (1) identify thermal-structural elements through parameter analysis, (2) validate findings via multisource data integration, and (3) reconstruct cross-sections revealing subsurface mineralization and fluid dynamics. This approach provides both detailed parameter identification and practical cross-section construction (Mukhamedyarov, 2013, 2016).

4.3. Thermal radiation and water saturation: Contour mapping and structural analysis

The surface thermal radiation field (60 m depth) reflects high-altitude temperature zoning, revealing an inverse correlation between altitude and temperature (Figs. 6d, e). Floodplain watercourses also present cool signatures, and while the relationship between water saturation and relief is less pronounced, higher elevations generally result in greater water saturation (Fig. 6f). The most hydrated areas are in the elevated plateau, which is linked to increased precipitation, whereas arid regions are found in the east and southeast. The water saturation pattern shows local anomalies, which are further explored in the mineral prospecting section (Fig. 6f).

To strengthen the summer–winter comparison illustrated in Fig. 6, a quantitative analysis of thermal radiation and water saturation parameters was conducted to assess seasonal variability and its implications for barite mineralization (Table 1; Fig. 6e–f). Pixel-based statistics computed from the summer and winter thermal datasets reveal distinct seasonal contrasts. The mean surface thermal radiation density during the dry season (April–May) is 10.42 W m^{-2}, whereas the wet-season (August–September) average decreases to 8.67 W m^{-2}, representing an approximate 17 % reduction associated with increased atmospheric moisture and ground wetness. The corresponding standard deviation declines from 1.12 W m^{-2} to 0.84 W m^{-2}, indicating more thermally uniform conditions under enhanced cloud cover and soil moisture.

Conversely, water saturation parameter values exhibit an opposite

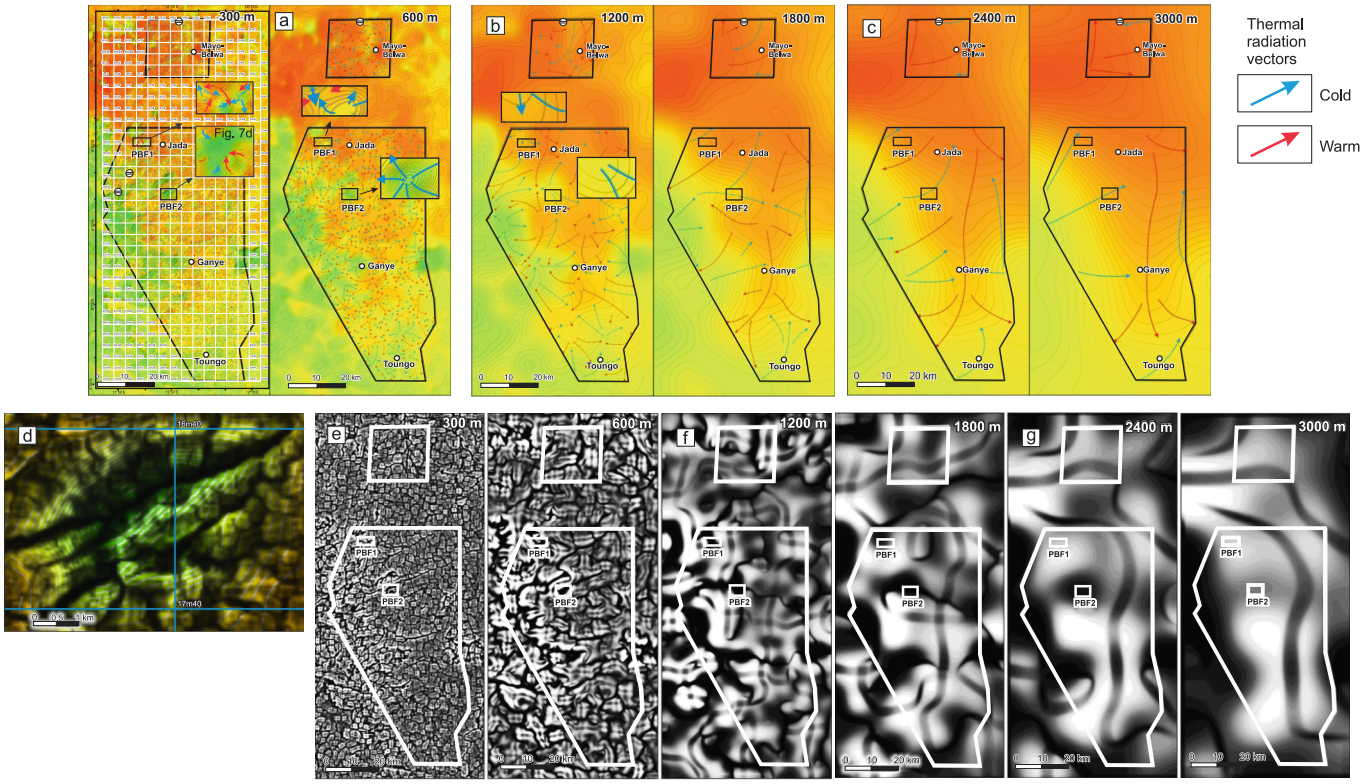

Fig. 7. Depth-dependent thermal radiation flux density distributions: (a) shallow anomalies (300–600 m depth); (b) intermediate depths (1200–1800 m), and (c) deep thermal patterns (2400–3000 m). (d) High-resolution block-cell structure of PBF2 at shallow depths (60–300 m), showing thermal field contours (green = cold, yellow = warm). (e–g) Block-cell structure of the thermal radiation at depths of (e) 300–600 m, (f) 1200–1800 m, and (g) 2400–3000 m, demonstrating the transition from fracture-controlled to conduction-dominated heat transfer.

trend, increasing by about 37 %, from a mean of 0.46 in the dry season to 0.63 in the wet season, consistent with intensified infiltration and reduced radiative heat flux. The strong negative correlation coefficient ($r = -0.72$) quantitatively supports the inverse relationship between thermal radiation and water saturation observed in Fig. 6d–f. Spatially, the highest dry-season anomalies (> 11.2 W m^{-2}) coincide with low water saturation zones around PBF2 and Ganye, whereas relatively cooler and more hydrated zones (> 0.7 WSP) occur across the elevated Mayo-Belwa plateau (Fig. 6d–f). These metrics substantiate the seasonal contrasts and demonstrate that barite mineralization is preferentially associated with stable thermal highs and moderately hydrated terrains. At 300 m depth, clear geothermal anomalies with distinct thermal highs and lows appear (Fig. 7a), suggesting a uniform heat source or equilibrium in an active hydrothermal system. The thermal highs likely correspond to fluid upwelling zones, and the cold vectors indicate fluid recharge or cooling. Between 300 and 600 m, thermal anomalies simplify, indicating a cooling system or a shift in dominant fluid convection zones (Irvine, 1989). Below 1,200 m, surface water signatures vanish, suggesting deeper fluid sources. At 1,800 m, distinct deep thermal anomalies in the northern sector likely reflect localized heat sources or fault-controlled fluid pathways, marking high-priority exploration targets (Tumanov, 2007). At 3,000 m, the thermal field simplifies with regional patterns of heat transfer, indicating a shift from fracture-controlled convection to conduction-dominated heat transfer. Exploration should focus on shallow zones for detailed targeting and deeper zones for regional resource assessments.The AICDS algorithm reveals a depth-dependent thermal architecture, with progressive simplification from shallow to deep zones (Fig. 7d–g). At 60–300 m, near-surface hydrothermal circulation is active, with fracture-controlled fluid pathways and potential mineralization boundaries. Deeper zones (300–1,800 m) show diminishing fracture influence, with regional heat sources becoming dominant (Sun et al., 2021). At 1,800–2,400 m, the thermal field marks a transition to conduction-dominated heat transfer, with the algorithm providing a tool for near-surface deposit targeting and depth cut-off indicators for hydrothermal viability (Tumanov, 2007; Mukhamedyarov, 2013, 2016). The water saturation distribution evolves with depth (Fig. 8a–g). At 300–600 m, a NW/SE dichotomy emerges, with a humid-to-dry ratio indicating deeper hydrological influences. At 1,200–1,800 m, the water saturation vectors become sparse, and at 2,400 m, a NE–SW humid vector intersects PBF1, suggesting a deep fluid conduit. At 3,000 m, the absence of vectors marks the hydrological base, beyond which conventional exploration may be ineffective. The 60–300 m water-saturated lineaments, when analysed with thermal data, show decoupled heat–fluid transfer mechanisms, suggesting active fluid–rock interactions and structural controls on groundwater circulation. These findings define key depth thresholds for mineralization processes and guide exploration strategies.

4.4. *Geodynamic schemes and structures*

The digital elevation model (DEM) reveals radial geodynamic stress patterns radiating from the Benue Trough (BT) toward adjacent cratons, particularly the Cameroon Volcanic Line (CVL), generating volcanic-like textures near the Congo Craton (Fig. 9a). These stresses form NW–SE-trending lineaments that intersect the dominant stress field, creating fault and fracture systems influenced by rock resistance and neotectonic deformation. Dominant NNE–SSW lineaments (fracture systems) and NW–SE stresses interact with subordinate NNE–SSW stresses, enhancing permeability through localized deformation and producing structural-thermochemical fluid pathways (Cox, 2020). The lineaments align with valley axes and include ENE–WSW, NNE–SSW, and NE–SW structures, many of which represent reactivated Pan-African shear zones. Notably, NE–SW faults now act as sinistral strike-slip faults due to Cretaceous deformation (Benkhelil, 1989; Guiraud et al.,

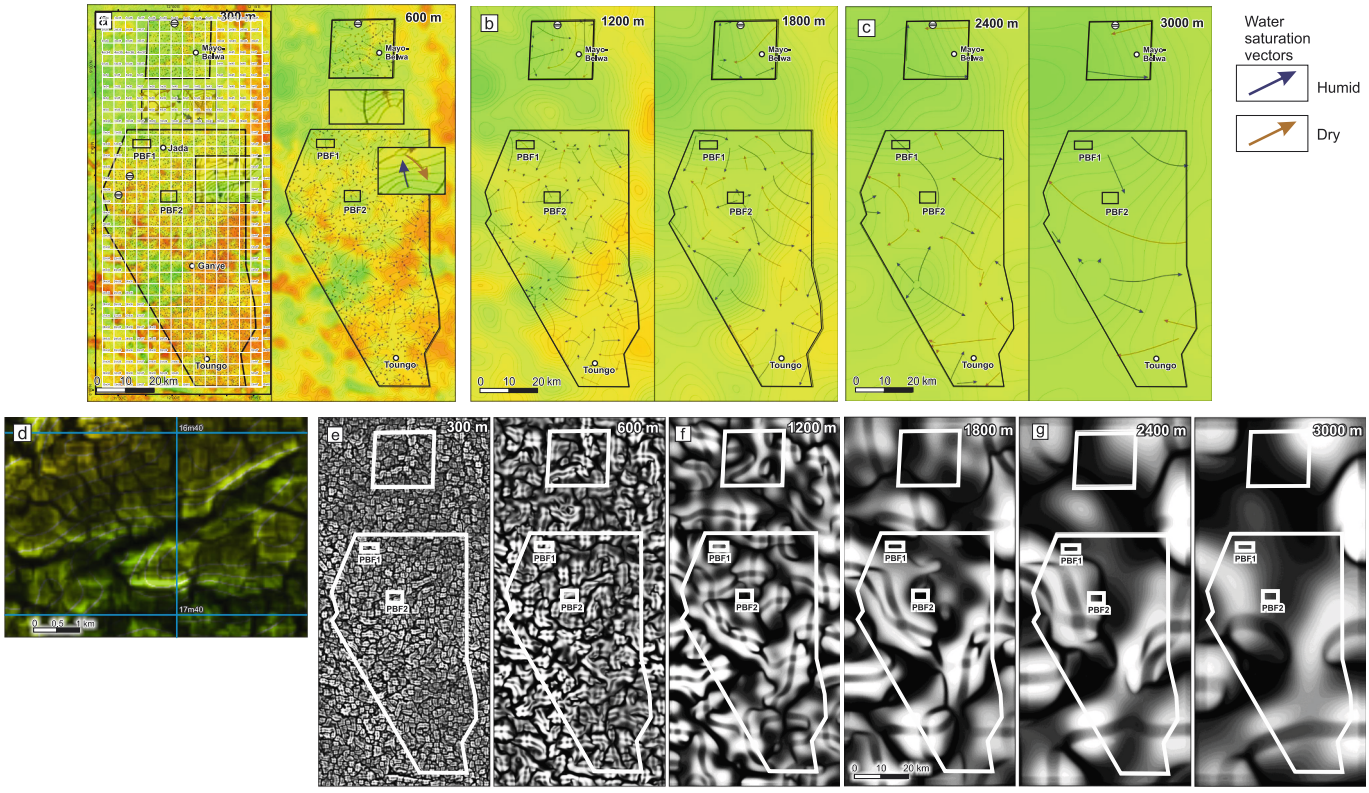

Fig. 8. Depth-dependent water saturation flux density distributions: (a) shallow anomalies (300–600 m depth); (b) intermediate depths (1200–1800 m), and (c) deep thermal patterns (2400–3000 m); (d) high-resolution block-cell structure of PBF2 at shallow depths (60–300 m), showing the field of relative water saturation contours (green = moisture, yellowish = dry); (e–g) block-cell structure of the field relative water saturation at depths of (e) 300–600 m; (f) 1200–1800 m, and (g) 2400–3000 m, demonstrating the transition from fracture-controlled fluid pathways to diffusion-dominated hydrological regimes with increasing depth.

1989), with barite mineralization controlled by perpendicular fracture sets along these faults (Fig. 9b). Rose diagrams confirm orientations consistent with oblique compression and rigid block fracturing, while tectonic stresses radiating from the trough shape complex relief and mountain chains (Fig. 9b).

The modern topography results from the interplay between lithological resistance to weathering and neotectonic deformation, including direction, magnitude, and structural contrast. Five principal neotectonic zones are defined on the basis of these factors (Table 2, Fig. 9b): (1) a deflection zone with extension and linear depressions in recent alluvium; (2) a low, uniform uplift zone with monoclinal warping of Mesozoic sediments; (3) a low, uneven uplift zone with ENE-tilted basement blocks; (4) an intense, even uplift zone with volcanic plateaus and syntectonic granitic slopes; and (5) an intense, uneven uplift zone with NNW-trending compression and relics of paleo-peneplains. Surface lithologies, from Cenozoic sediments to Precambrian crystalline rocks, align with these neotectonic domains, reflecting differential weathering and structural forcing (Dada et al., 2024).

Various lineament patterns reflect different geotectonic stress conditions, which are influenced by the type and direction of tectonic forces (Dobretsov et al., 2013). In the study area, compression in a shift zone is marked by narrow fault zones subjected to compressive forces (Fig. 9c) (Kamaunji et al., 2022a). Crushing between rigid blocks creates uniform directional stress, whereas compression above a dome results in the formation of multiple fractures in a circular region (Fig. 9c). Compression above a shaft results in linear fractures above vertical geological features (Fig. 9c). Scattered compression shows random stress patterns, whereas stretching above a reset zone indicates expansion and tension along a reset fault. Oblique compression involves forces acting at an angle, causing both horizontal and vertical deformation.

5. Discussion

5.1. Barite mineralization via thermal infrared (TIR) spectroscopy

Thermal infrared data from Landsat-7 ETM + Band 6 highlight key features of the barite fields (PBF1 and PBF2) (Fig. 9d). PBF1, located between Mayo-Belwa and Jada, shows a distinct thermal anomaly, likely due to exothermic barite precipitation, heat retention by barite-rich rocks, and possible hydrothermal activity. Its sharp, elliptical shape suggests structurally controlled mineralization along fault zones, akin to barite-rich epithermal systems in Nevada's Great Basin (Nash, 1996; Calvin et al., 2015), and geothermal-linked barite mineralization in Sudan's Red Sea Hills (Daoud et al., 2025). PBF2 has a weaker thermal signal, possibly reflecting lower mineralization temperatures, variable barite purity, or thicker overburden, similar to barite-bearing alteration zones detected under alluvium in Nigeria's Benue Trough (Oha et al., 2021). Thermal imagery reveals structural controls on barite emplacement, with anomalies aligned with faults and fractures that channelled mineralizing fluids (Schleicher et al., 2009). Similar patterns were observed in NW Iran, where ASTER data identified barite veins linked to fault zones (Behyari et al., 2019). These thermal signatures also highlight lithologic contacts that may have influenced mineralization. For exploration, Landsat-7 Band 6 and Landsat-8 Bands 10–11 help map prospective zones, structural controls, and barite deposit types on the basis of thermal response (USGS, 2019a; Rani, 2025).

Ground-truth validation of Landsat-7 ETM + TIR data was conducted using a calibrated FLIR TG267 infrared thermometer (±1.5 °C accuracy, 8–14 μm range) at 15 sites across barite zones (PBF1, PBF2) and background areas. Measurements (60 m × 60 m, matching Landsat resolution) were synchronized with satellite overpass (10:30 AM local time), averaging 3–5 replicates to account for microvariability. The recorded temperatures ranged from 28.5 °C (background) to 42.3 °C (barite

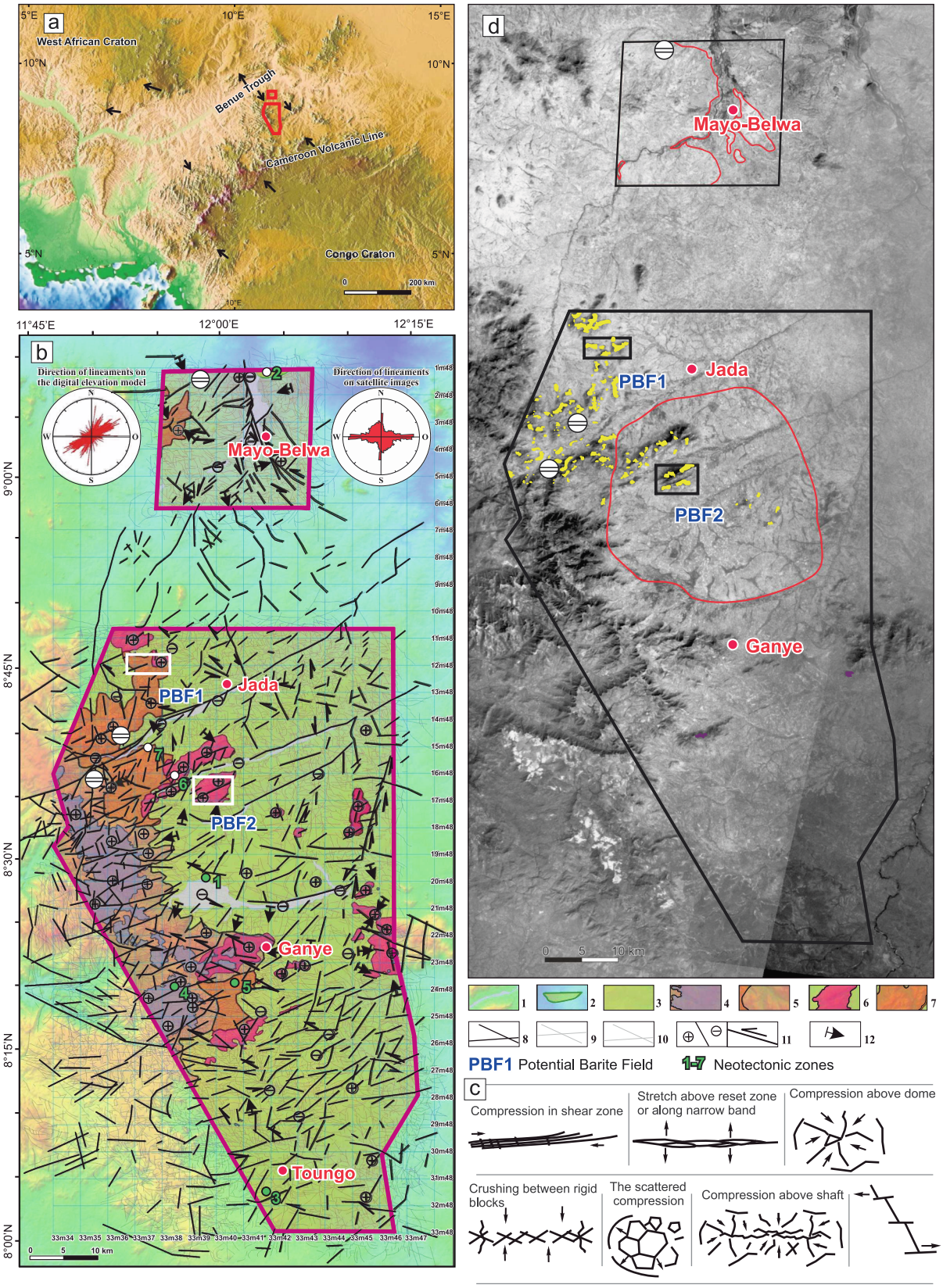

Fig. 9. (a) Study area location (digital elevation model); (b) Geodynamic zoning scheme showing the following: 1–7 = neotectonic zones/subzones (Table 2), 8–10 = faults (8: DEM-derived, 9: thermal band 6-derived, 10: water saturation-derived), 11–12 = tectonic displacement and stress directions; (c) Lineament patterns resulting from different geotectonic stress situations. The arrows indicate the direction of tectonic stress, which leads to various geological features, such as compression zones, stretching, and oblique deformation. (d) Barite reflectance (thermal cold conductive anomalies) overlaid on Band-6 thermal infrared imagery, highlighting potential barite fields (PBF).

Table 2
Geodynamic zoning and neotectonic characteristics of the study area.

Zone Name	Sub zone	Surface Lithology	Neotectonic Regime	Dominant Structures	Fig. 9b Ref.	Cloud Cover (%), USGS, 2019b
Deflection Zone	–	Modern alluvial deposits	Extension-dominated	Linear depressions	1	<5%
Low Uniform Uplift	–	Mesozoic sediments, alluvial and lacustrine deposits	Transitional	Monoclinal structures (southern Benue Trough margin)	2	~10 %
Low Uneven Uplift	–	Precambrian basement (gneisses, migmatites, schists, amphibolites, granites);Cenozoic sediments (Neogene proluvium)	Transitional	ENE-tilted plate with low-amplitude ridges and ENE-trending valleys	3	<12 %
Intense Even Uplift	A	Late Cretaceous-Miocene basic/ultrabasic/alkaline volcanics	Compression with local extension	Elevated volcanic plateau (peneplain surface)	4	<8%
	B	Precambrian syntectonic granites, migmatites, gneisses	Compression with local extension	Steep plateau margins	5	<10 %
Intense Uneven Uplift	A	Late Precambrian post-tectonic granites with schist/amphibolite xenoliths	Strong NW-SE compression	ENE-trending uplifted blocks (relict peneplain surfaces)	6	<7%
	B	Precambrian syntectonic granites, migmatites, gneisses	Latitudinal/all-direction compression	Submeridional uplifted blocks (preserved peneplain relics)	7	<10 %

zones), reflecting exothermic mineralization and the low thermal conductivity of barite. GPS-georeferenced data paired with surface metadata (lithology, soil type) yielded an RMSE of ± 1.2 °C between FLIR and Landsat-derived LSTs, confirming satellite reliability. Notably, the FLIR peaks (>40 °C) aligned with high thermal flux densities (e.g., 12,030 W/m^2 at PBF4, Fig. 6e), validating the combined point-source (thermometer) and areal (Landsat/flux) thermal analysis for barite exploration.

5.2. Potential barite fields based on integrated geospatial data

The barite prospects PBF1 and PBF2 exhibit distinct mineralization indicators through their thermal and hydrological signatures (Fig. 6d–f). PBF1 has strong hydrothermal characteristics (60–80 °C subsurface); FLIR's > 40 °C surface anomalies in barite zones matches this high subsurface estimate. This is consistent with fluid-saturated geothermal systems such as China's Sulu belt (Wang et al., 2016), and follows empirical radiation–temperature relationships (Blackwell et al., 2011). In contrast, PBF2 shows lower thermal radiation values (40–60 °C), comparable to fracture-controlled deposits in Morocco's Atlas (Samaoui et al., 2023) under conductive heat transfer models (Jaupart and Mareschal, 2007). Moderate FLIR readings (~35 °C) in PBF2 correspond to the PBF2′s lower modelled range (40–60 °C), suggesting discrete heat sources within 25–30 °C/km geothermal gradients (Wagner et al., 2005). PBF1′s high water saturation (70–90 %) facilitates Ba-rich fluid deposition (Hanor, 1969; Orywall et al., 2017), whereas PBF2′s moderate saturation (50–70 %) indicates fracture-focused mineralization (Kronyak et al., 2019). This is similar to paleo-geothermal systems in California's Noble Hills granite (Klee et al., 2021). Notable, the temperature estimates (60–80 °C for PBF1 and 40–60 °C for PBF2) were derived by converting the map's flux thermal radiation values (in W/m2·μm·sr, cf. Fig. 6e) using established geothermal gradients of 25–30 °C/km (Turcotte and Schubert, 2014).

5.3. Geodynamic zoning and neotectonic controls on barite mineralization

The Mayo-Belwa barite fields (PBF1, PBF2) show distinct spatial relationships with geodynamic zones and neotectonic structures, as revealed by digital elevation models and lineament analysis (Figs. 6d, 9b; Table 2). These fields occur within different structural domains of the Eastern Nigerian Basement that control mineralization. PBF1 occupies a deflection zone with two subzones: Subzone A contains late Precambrian post-tectonic granites with schist/amphibolite xenoliths deformed by NW–SE compression, forming ENE-trending uplifted blocks hosting fracture-controlled barite veins (Fig. 9b; Table 2); Subzone B comprises Precambrian syntectonic granites, migmatites and gneisses under latitudinal/all-direction compression, creating submeridional uplifted blocks that localize mineralization at structural intersections (Fig. 9b; Table 2). PBF2 occurs in Zone 6 (Subzone A) of the Intense Uneven Uplift domain, comprising late Precambrian post-tectonic granites with schist/amphibolite xenoliths (Fig. 9b; Table 2). These xenoliths serve dual roles as both brittle fracture conduits and barium sources, while their sulfide-rich zones may locally reduce sulfide, creating complex mineral assemblages. NW–SE compression has formed ENE-trending uplifted blocks (relict peneplains) that channel fluids along reactivated basement structures. Mineralization is fracture-controlled, with barite veins concentrated at ENE-trending faults and NNW fracture intersections.

The scarcity of barite in Zone 1 (alluvial deflection zone) and Zone 2 (low uniform uplift) (Fig. 9b) suggests that active sedimentation and monoclinal structures hinder barite preservation. Two primary factors explain this phenomenon: (1) clastic sedimentation dilutes Ba-rich fluids (Hanor, 2000), and (2) reducing conditions convert barite ($BaSO_4$) to sulfide (Griffith and Paytan, 2012). While high sedimentation can preserve barite (e.g., the Peru margin (Torres et al., 1996), exceptions occur in hydrothermal vent-proximal (Guaymas Basin; Kastner and Siever, 1983; Teske, 2020), or rapidly buried settings (e.g., Black Sea, Henkel et al., 2012). Monoclines typically lack fracture density for fluid focusing (Tranter et al., 2021), although barite may form where faults disrupt them (e.g., High Atlas, Morocco, Nait-Bba et al., 2024). Cold conductive signatures (Fig. 10) effectively identify potential barite fields (PBF1-PBF2), with violet conductive objects marking barite-associated fracture networks in resistive host rocks. While barite ($BaSO_4$) is electrically resistive (Hong et al., 2022), its deposition in sulfide–clay-rich altered zone creates conductive halos (Melekestseva et al., 2014). These anomalies aligned with NE–SW structural trends, likely highlighting Precambrian–Cenozoic fracture-controlled mineralization.

5.4. Integration of Landsat temperature resolution and confidence assessment for barite field thermal anomalies

The thermal anomalies associated with barite fields PBF1 and PBF2, as synthesize in Table 3, were interpreted and their reliability assessed using a dual-parameter approach that integrates the fundamental sensitivity limit of the data with signal robustness metrics. The confidence that a detected anomaly represents a genuine geophysical signal, rather than system noise, was determined by benchmarking against the Landsat temperature resolution threshold (ΔT_k). This parameter, which defines the minimum detectable temperature contrast for a given processing layer (N), was calculated using the empirical relationship $\Delta T_n = 0.2/N^{2.5}$ (Mukhamedyarov, 2016; Table 4), where the layer number is

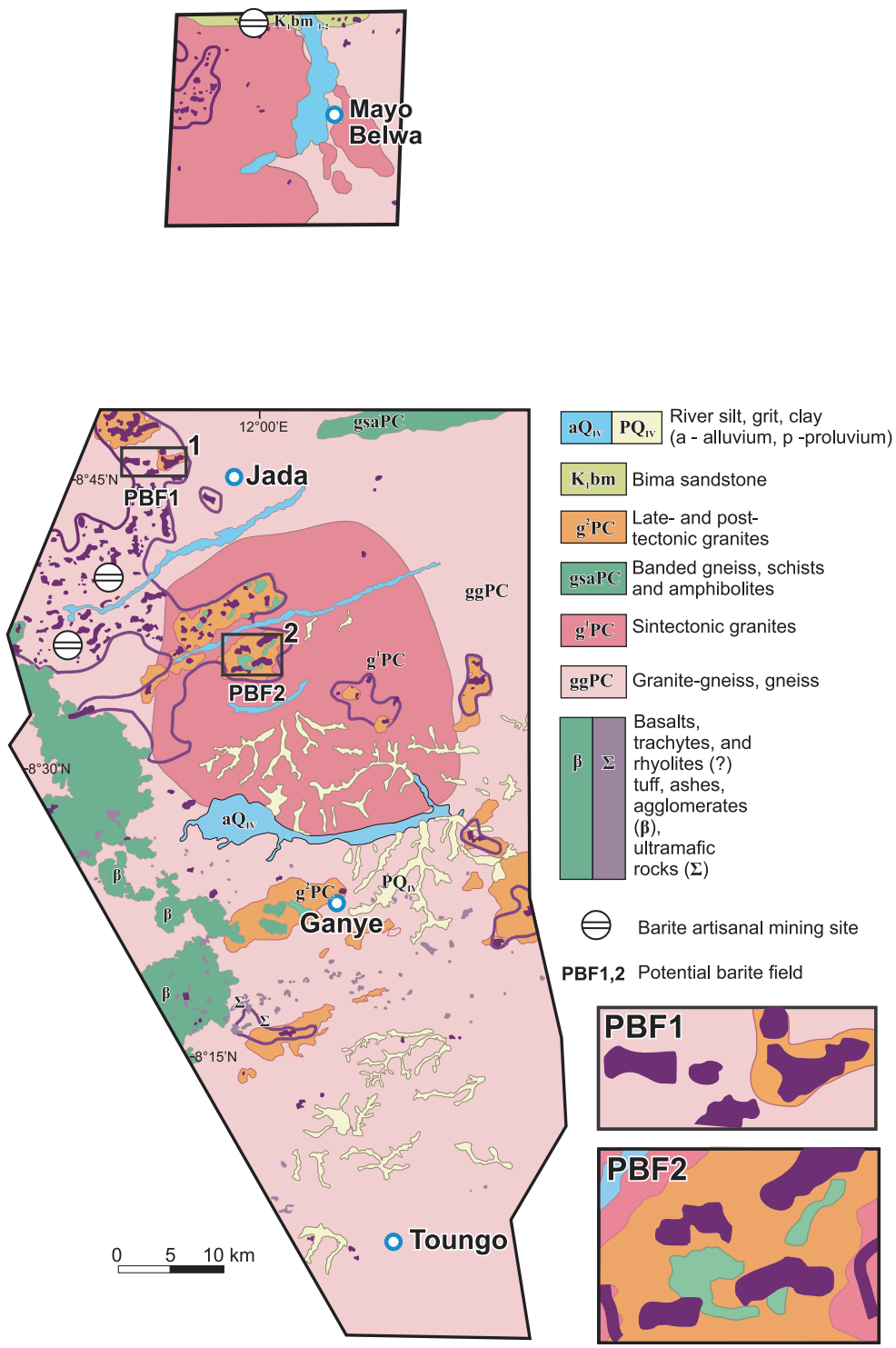

Fig. 10. Spatial distribution of cold conductive anomalies, with violet spots marking discrete conductive objects and violet contours delineating anomaly boundaries. The black circles indicate artisanal barite mining sites for field verification.

determined by the anomaly's depth. This established ΔT_k serves as a deterministic confidence threshold.

The robustness of each anomaly was further quantified by its Signal-to-Noise Ratio (SNR), calculated as SNR = ΔT / N, where the noise level (N) was derived from the standard deviation of the thermal signal in geologically inert background areas. For instance, the robust anomaly of 1.2 K in PBF1 at 300 m depth (SNR = 2000:1) has a calculated noise level of 0.0006 K. To account for potential minor systematic uncertainties in the TGM algorithmic processing, a conservative precision estimate of ± 0.05 K was applied across all measurements. Crucially, even with this margin, all detected anomalies remain statistically significant and vastly exceed their detection limits.

The implications derived from this integrated analysis are clear. For PBF1 at 300 m (Layer 10, $\Delta T_k = 6.0 \times 10^{-}4$ K), the high ΔT (1.2 K) and exceptional SNR (2,000:1)—which is three orders of magnitude above the sensitivity threshold—confirm it as a Robust target (Table 3), consistent with the sharp thermal boundaries and optimal depths defined in Table 6. The persistence of a significant anomaly (ΔT = 0.3 K)

Table 3
Synthesis of barite field thermal signatures, showing observed thermal anomalies (ΔT) contextualized against the method-specific sensitivity threshold (ΔT_k). The ΔT_k values, derived from Mukhamedyarov (2016), represent the minimum detectable temperature contrast for each depth layer and serve as a deterministic confidence threshold. All observed signals significantly exceed their corresponding sensitivity thresholds, confirming they are robust geophysical features.

Field	Depth (m)	Observed ΔT (K)	Signal-to-NoiseRatio (SNR)	Sensitivity Threshold ΔT_k (K)	Implication
PBF1	300	1.2	2,000:1	$6.0 \times 10 - 4$	Robust target
PBF1	1,200	0.3	2,700:1	$1.1 \times 10 - 4$	Persistent system
PBF2	1,800	0.08	2,000:1	$4.05 \times 10 - 5$	Lower-T mineralization
PBF2	3,000	0.05	2,500:1	$1.97 \times 10 - 5$	High-risk, needs validation

Table 4
Temperature Sensitivity Resolution in Landsat Layers (Mukhamedyarov, 2016).

N	ΔT_k (K)	N	ΔT_k (K)	N	ΔT_k (K)
1	0.2	21	9.9×10^{-5}	41	1.85×10^{-5}
2	3.5×10^{-2}	22	8.8×10^{-5}	42	1.74×10^{-5}
3	1.9×10^{-2}	23	7.8×10^{-5}	43	1.64×10^{-5}
4	6.25×10^{-3}	24	7.1×10^{-5}	44	1.55×10^{-5}
5	3.6×10^{-3}	25	6.4×10^{-5}	45	1.47×10^{-5}
6	2.3×10^{-3}	26	5.8×10^{-5}	46	1.39×10^{-5}
7	1.5×10^{-3}	27	5.4×10^{-5}	47	1.32×10^{-5}
8	1.1×10^{-3}	28	4.8×10^{-5}	48	1.25×10^{-5}
9	8.2×10^{-4}	29	4.4×10^{-5}	49	1.18×10^{-5}
10	6.0×10^{-4}	30	4.05×10^{-5}	50	1.13×10^{-5}
11	5.9×10^{-4}	31	3.88×10^{-5}	51	1.07×10^{-5}
12	4.6×10^{-4}	32	3.85×10^{-5}	52	1.002×10^{-5}
13	3.3×10^{-4}	33	3.22×10^{-5}	53	9.7×10^{-6}
14	2.7×10^{-4}	34	3.01×10^{-5}	54	9.3×10^{-6}
15	2.3×10^{-4}	35	2.75×10^{-5}	55	8.9×10^{-6}
16	1.9×10^{-4}	36	2.57×10^{-5}	56	8.5×10^{-6}
17	1.7×10^{-4}	37	2.4×10^{-5}	57	8.1×10^{-6}
18	1.45×10^{-4}	38	2.24×10^{-5}	58	7.7×10^{-6}
19	1.3×10^{-4}	39	2.1×10^{-5}	59	7.4×10^{-6}
20	1.1×10^{-4}	40	1.97×10^{-5}	60	7.1×10^{-6}

The table lists temperature resolution thresholds (ΔT_k) for Landsat layers 1–60, derived from $\Delta T_n = (\delta_n/\delta_k)^{2.5} = 0.2/N^{2.5}$, showing exponentially decreasing sensitivity with depth (higher N). These ΔT_n values govern vertical resolution, with Layer N = 15 ($\Delta T_n = 2.3 \times 10^{-4}$°C) selected as optimal for barite exploration (see Section 3.1).

with an even higher SNR (2,700:1) at 1,200 m depth (Layers 22–23) indicates a Persistent system. For PBF2, the weaker anomalies at 1,800 m (Layer 30) and 3,000 m (Layer 40), while still possessing strong SNRs (2,000:1 and 2,500:1) and clear exceedance of their ΔT_k thresholds, suggest Lower-T mineralization and a High-risk target that requires validation, a finding aligned with PBF2's subdued thermal markers summarized in Table 5.

The finding that all observed thermal signals exceed their layer-specific sensitivity thresholds by more than three orders of magnitude confirms they are genuine features, robustly distinguishable from system noise. This validates the TGM's capability to resolve low-amplitude thermal features associated with deep-seated mineralization, a capability further demonstrated by the specific algorithms (e.g., AICDS, VT/IVD/2VD) that successfully mapped the structural and fluid pathways for both PBF1 and PBF2, as detailed in Table 5.

5.5. Prospectivity mapping of potential barite fields (PBF)

5.5.1. Potential barite field 1 (PBF1): Taso and Tola deposits

The Taso deposit, hosted in Pre-Cambrian granite–gneiss and last- to post-tectonic granites (Fig. 10, Table 4), shows a strong correlation between cold conductive anomalies and high ∇T (dry)/low W zones (Fig. 11a). lines mark axial conductive heat zones (dense, dry rocks), whereas the dark violet lines indicate cold dry objects linked to barite mineralization (Fig. 11a). The GS algorithm improved the anomaly contrast by isolating thermal deviations ($|T(x,y,z) - \mu T| > 2\sigma T$), especially in granite–gneiss contacts (Fig. 11a). Convective warm (red dotted lines) and cold flows (blue lines) follow valleys and slopes, marking fluid pathways (Fig. 11a). A potential mineralized body extends to 540 m (Fig. 11b). The LT algorithm mapped the thermal radiation density (Td (x,y,z)), revealing the low diffusivity ($\Delta Td < 0.1$ W/m^2) of barite in the central vein.

Table 5
Exploration parameters and algorithms for PBF1 and PBF2.

Parameter	PBF1 (Taso & Tola)	PBF2 (Yebbe, Zeibei, Ngurore)
Optimal Depths	180–300 *m*	60–300 *m*
Host Rocks	Pre-Cambrian granite-gneiss (Taso); granitoids with metasedimentary xenoliths (Tola).	Precambrian banded granitoids with amphibolite xenoliths
Key Structures	ENE-striking veins; "house-shaped" anomalies	Propeller-shaped (Ngurore); vertical reorientation (Zeibei)
Thermal Markers	$\partial T/\partial z > 0.6$ K/m; $\partial^2 T/\partial z^2 < -0.3$ K/m^2	$\nabla T > 0.8$ K/m (Yebbe); Td < 0.08 W/m^2 (Ngurore)
Fluid Indicators	W < 0.2 (dry zones)	W > 0.3 (endogenous inflows at 0.8–4 km)
Algorithms Applied		
• AICDS	Discriminated mineralization (W thresholds)	Identified false anomalies (seasonal riverbeds)
• VT/1VD/2VD	Prioritized high-gradient sections (GT > 0.5 K/m); mapped boundaries ($\partial^2 T/\partial z^2$ minima)	Resolved vertical reorientation (Zeibei); validated fluid conduits
• LT/GS	Mapped low-diffusivity barite ($\Delta Td < 0.1$ W/m^2)	Correlated Td/W anomalies (Ngurore base)
Drill Programs	2–4/220, 2–5/300 wells (220–300 m)	205 m holes (Zeibei/Ngurore); 206 m (Yebbe)

A cross-section of the object, overlaid on the 2nd derivative of water saturation and an autogenerated block-cell structure, is shown in a vertical incision of 12 m37 (Fig. 12a). The AICDS algorithm identified a probable mineralized vein with a "house-shaped" thermal anomaly beneath dry, cold thermal vectors (Fig. 12a). The thermal radiation and water saturation thresholds suggest that the entire watershed is viable, with an axial zone (dark block-cell lineaments) prospective for barite. The VT algorithm prioritized this section because of high thermal gradients ($GT(x,y,z) > 0.5$ K/m), revealing westwards drift of the mineralized body (Fig. 12a). The Tola deposit, hosted in Pre-Cambrian granitoids with metasedimentary xenoliths, exhibits only its eastern border (105 m long at 60 m depth) in a mountainous zone (961 m relief) (Fig. 12b). Boundaries were delineated by overlaying thermal anomalies (ΔT) and low water saturation ($W(x,y,z) < 0.2$) on Google Earth imagery via TGM outputs. At 120 m depth, two zones emerge (east: 345 m; central: 300 m), merging into a 1905 m ENE-striking body by 240 m (Fig. 12b). The GS algorithm highlights this elongation as a high-contrast anomaly ($C(x,y,z) > 1.8\sigma T$), with lineaments autotraced from gradients ($\nabla T > 0.5$ K/m) and verified against Landsat trends. These align with fracture density (Fig. 12a) and AICDS-classified cell blocks, which filter false anomalies via thermal inertia thresholds ($\Delta T/\Delta t <$ 0.05 K/day). Below 300 m, the strike shifts NNE, which correlates with a lower fracture density and weaker anomalies ($\Delta T \approx 0.08$ K).

The 1VD and 2VD algorithms identified sharp thermal boundaries ($\partial T/\partial z > 0.6$ K/m; $\partial 2T/\partial z2 <$ -0.3 K/m2) at 180–300 m depths (Fig. 12c), confirmed by vertical scaling (0.18–0.3 km Alt. km axis) and peak gradients at drillhole 12 m38 (Fig. 12c). The inflection points ($\partial 2T/\partial z2 <$ -0.3 K/m2) marked fluid conduits, with lateral anomaly continuity (2.5–5 km scale) indicating structural controls (Fig. 12c). This

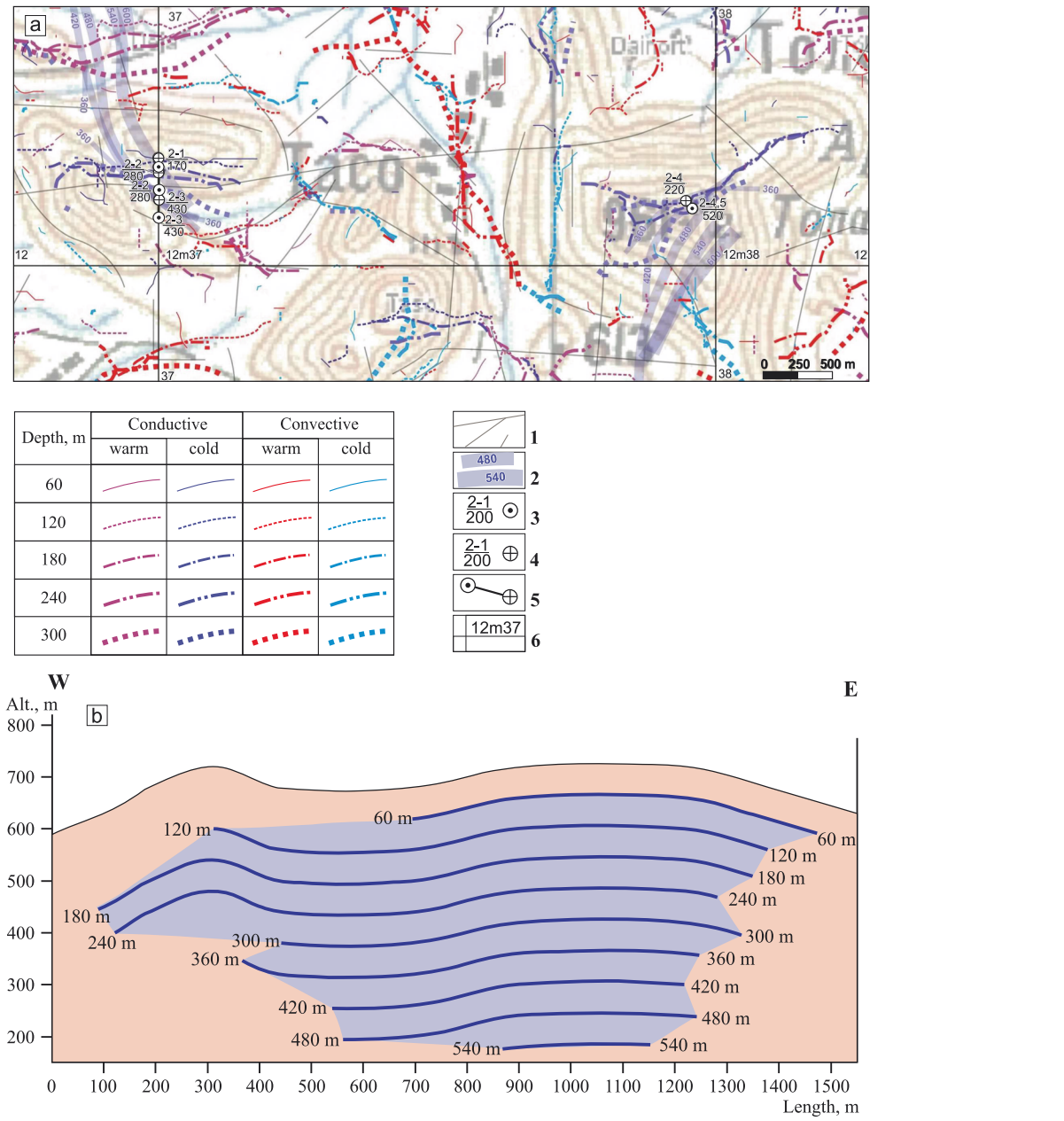

Fig. 11. (a) Heat transfer mechanisms in potential barite field 1 (PBF1) showing (1) water saturation-derived lineaments, (2) deep conductive cold objects (>300 m depth), (3) wellheads with site/well numbers (above line) and drift lengths (below line), (4) well bottoms (matching wellhead numbers), (5) surface projections of wells, and (6) numbered vertical section lines. (b) Cross section of the Taso ore body (PBF1) showing structural controls on mineralization.

links surface block-cell structures (Fig. 12a) to ENE-striking Tola mineralization (Fig. 12b), highlighting the vertical resolution of TGM. The vertical orientation of the eastern segment (Fig. 12b) matches the tectonic stress patterns (Fig. 9b), as verified by the VT algorithm's selection of high-gradient sections (GT(x,y,z) > 0.4 K/m). The LT algorithm detected low water saturation (W(x,y,z) < 0.2) in the NNE segment, explaining the anomaly attenuation (Fig. 12d). Drill clusters (2–4/220 at 220 m and 2–5/300 at 300 m) and reservoir cross-sections appear in Fig. 12d and are aligned with the 12 m38 drill line (Fig. 12c). Three key markers define the 220–300 m target: 2–5/295 represents the peak thermal anomaly ($\nabla T > 0.8$ K/m at 295 m; Fig. 12c), 2–4/220 represents the mineralized upper boundary ($\partial T/\partial z > 0.6$ K/m), and 2–5/300 represents the mineralization base ($\partial 2T/\partial z2 < -0.3$ K/m2 at 300 m; Fig. 12d). PBF1 validation confirmed the accuracy of TGM in resolving sub 300 m vein geometries via 'house-shaped' anomalies and fracture patterns (Fig. 12a, c-d).

5.5.2. Potential barite field 2 (PBF2): Yebbe, Zeibei, and Ngurore deposits

The Yebbe–Zebei–Ngurore southern uplands (PBF2) feature mountainous terrain (600 m elevation) with NNW-trending faults (Fig. 13a). It is hosted by syn-, late- and post-tectonic granites (Fig. 10). Like PBF1, the coloured lines denote heat transfer mechanisms at a depth of 300 m (Fig. 13b): crimson for dry conductive zones (180–300 m), dark violet for barite deposits, blue for cold convective valley flows, and light pink for deep warm fluids. Seasonal riverbeds (W(x,y) > 0.3 in March vs. < 0.2 in Oct/Nov) were excluded as false anomalies via the AICDS. The GS algorithm identified high-magnitude anomalies (A(x,y,z) > 3σT) in dense (>2.69 g/cm^3) banded granitoids (drillhole-validated16), with ΔT ≈ 0.08–0.12 K in the Landsat B6 data. These features align with NNW–SSE banding and 1800–2400 m elevation breaks at 11°59′48.85″N, 9°35′59.41″E (DigitalGlobe, Fig. 13b).

The Yebbe deposit occurs in Precambrian granitoids (1080–920 m ASL) with metasedimentary xenoliths, following ENE structures (35°

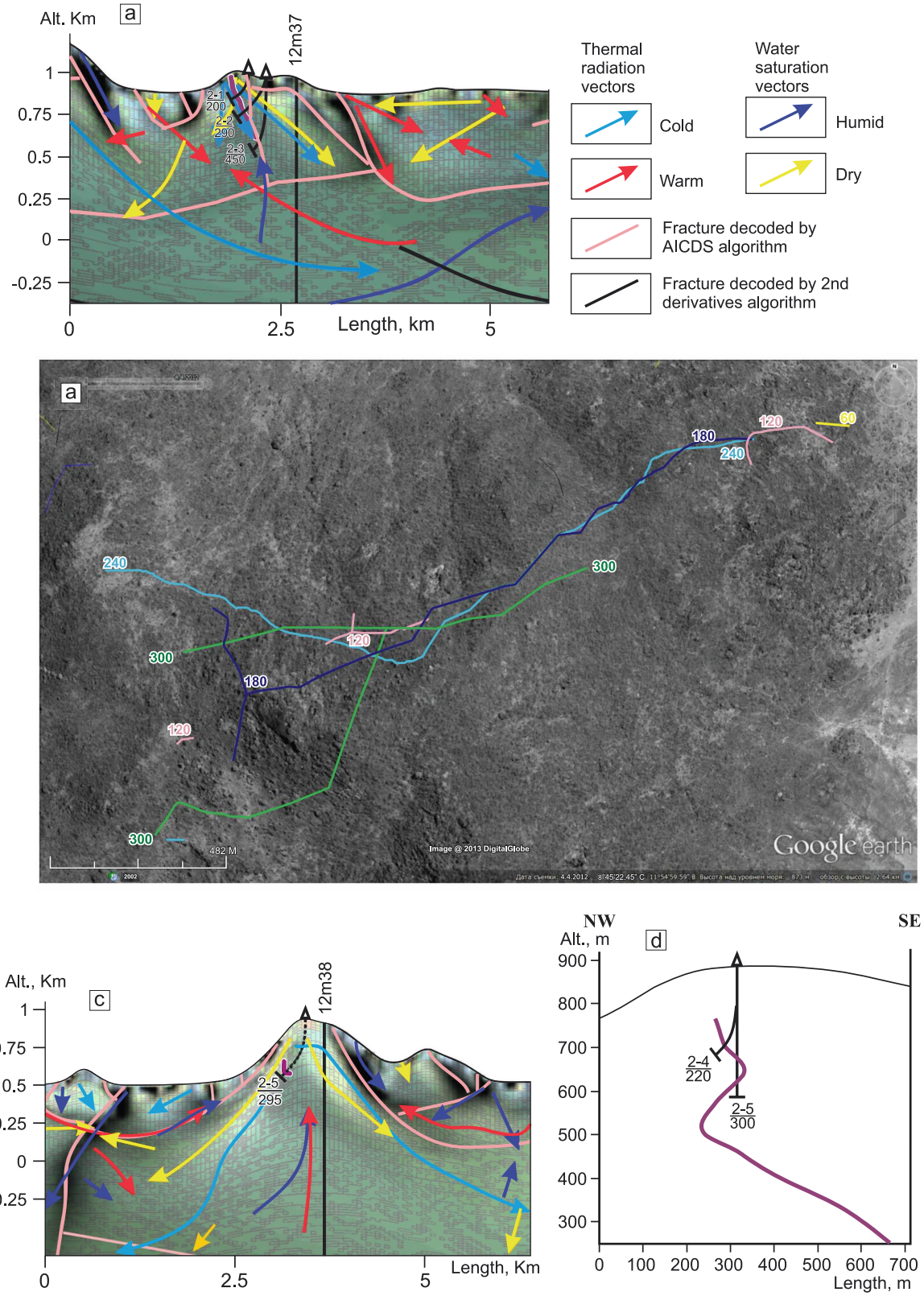

Fig. 12. (a) Cross-section of the Taso ore body (PBF1) reveals an AICDS-generated "house-shaped" thermal anomaly beneath dry/cold vectors, with block-cell lineaments delineating prospective axial zones ($\nabla T > 0.5$ K/m). Color-coded vectors indicate thermal properties (red = heat, blue = cold, yellow = aridity, violet = water saturation) and faults (pink/black), whereas well data show site/well numbers (above line) and drift lengths (below line). (b) The Tola ore body, hosted in Precambrian granitoids, displays progressive development from a 105 m eastern boundary at 60 m depth to a 1905 m ENE-striking body at 240 m depth ($C(x,y,z) > 1.8\sigma T$), overlain on Google Earth imagery. (c) The 180–300 m high-gradient zone ($\partial T/\partial z > 0.6$ K/m) contains drill-confined mineralization boundaries, including a peak thermal anomaly at 295 m ($\nabla T > 0.8$ K/m) and the base of economic mineralization at 300 m ($\partial^2 T/\partial z^2 < -0.3$ K/m^2). (d) Optimized well clusters (2–4/220, 2–5/300) target NNE-striking mineralization.

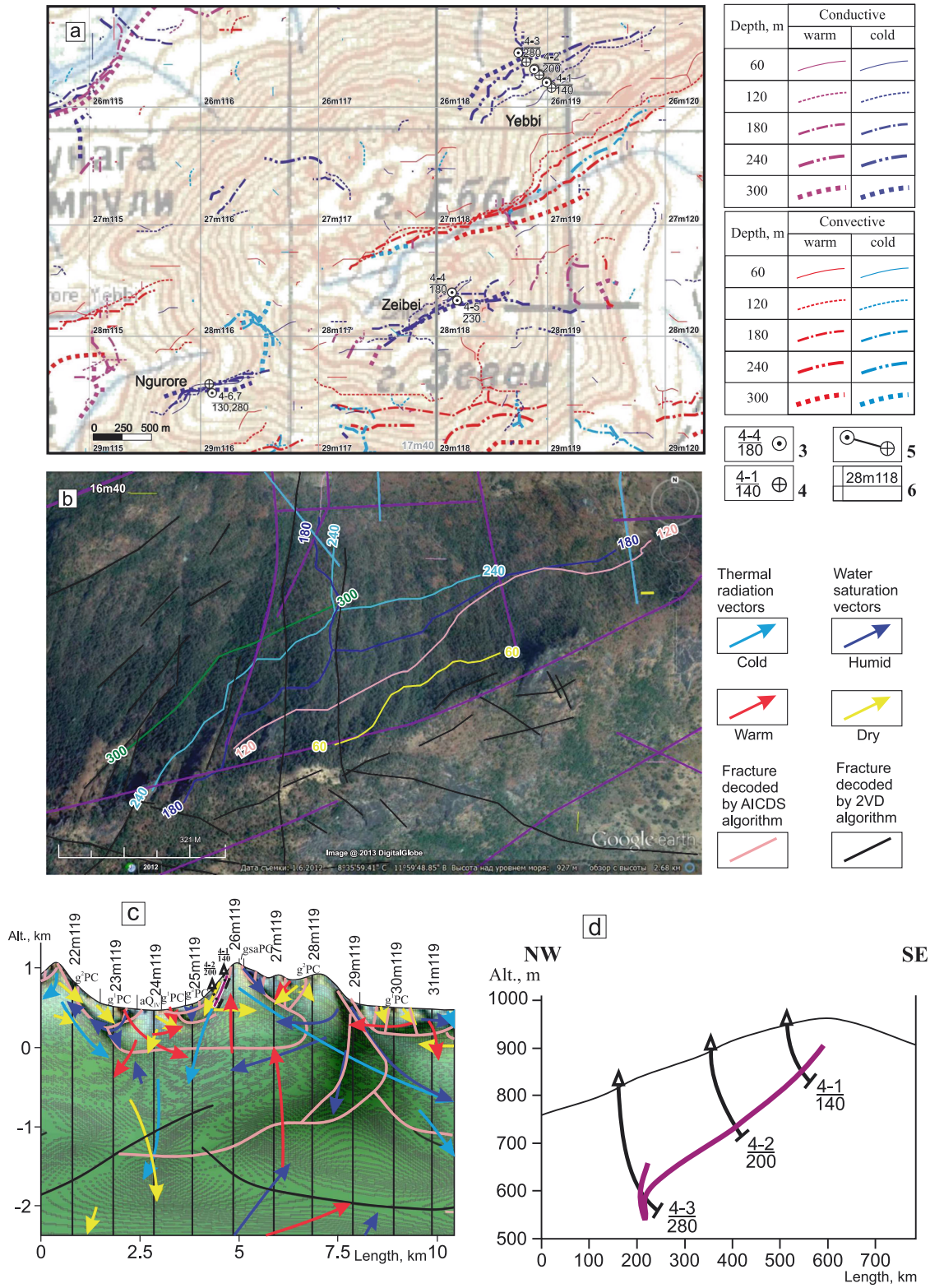

Fig. 13. (a) Heat transfer mechanisms in potential barite field 2 (PBF2), with symbols consistent with those in Fig. 12. (b) Spatial distribution of the Yebbe ore body (60–300 m depth) overlain on Google Earth imagery, showing decoded lineaments: black (Google-derived), crimson (Landsat Band 6 conductive zones), and blue (Landsat water-saturated channels). The deposit exhibits ENE-trending mineralization (35° WNW dip) within Precambrian granitoids, expanding from 610 m (60 m depth) to 2,360 m (180 m depth) before contracting to 750 m (300 m depth); (c) Cross-section highlighting AICDS-decoded fractures and descending dry vectors controlling mineralization, with high-gradient zones ($|\nabla T| > 0.8$ K/m) at 120 m depth. (d) Recommended drill holes (4–1/140 m, 4–2/200 m, and 4–3/280 m) targeting shallow thermal anomalies ($\Delta T \approx 0.08$ K), fluid influx boundaries ($\partial W/\partial z > 0.1$ m^{-1}), and deep fracture zones ($\partial^2 T/\partial z^2 < -0.3$ K/m^2) along NNW-oriented faults.

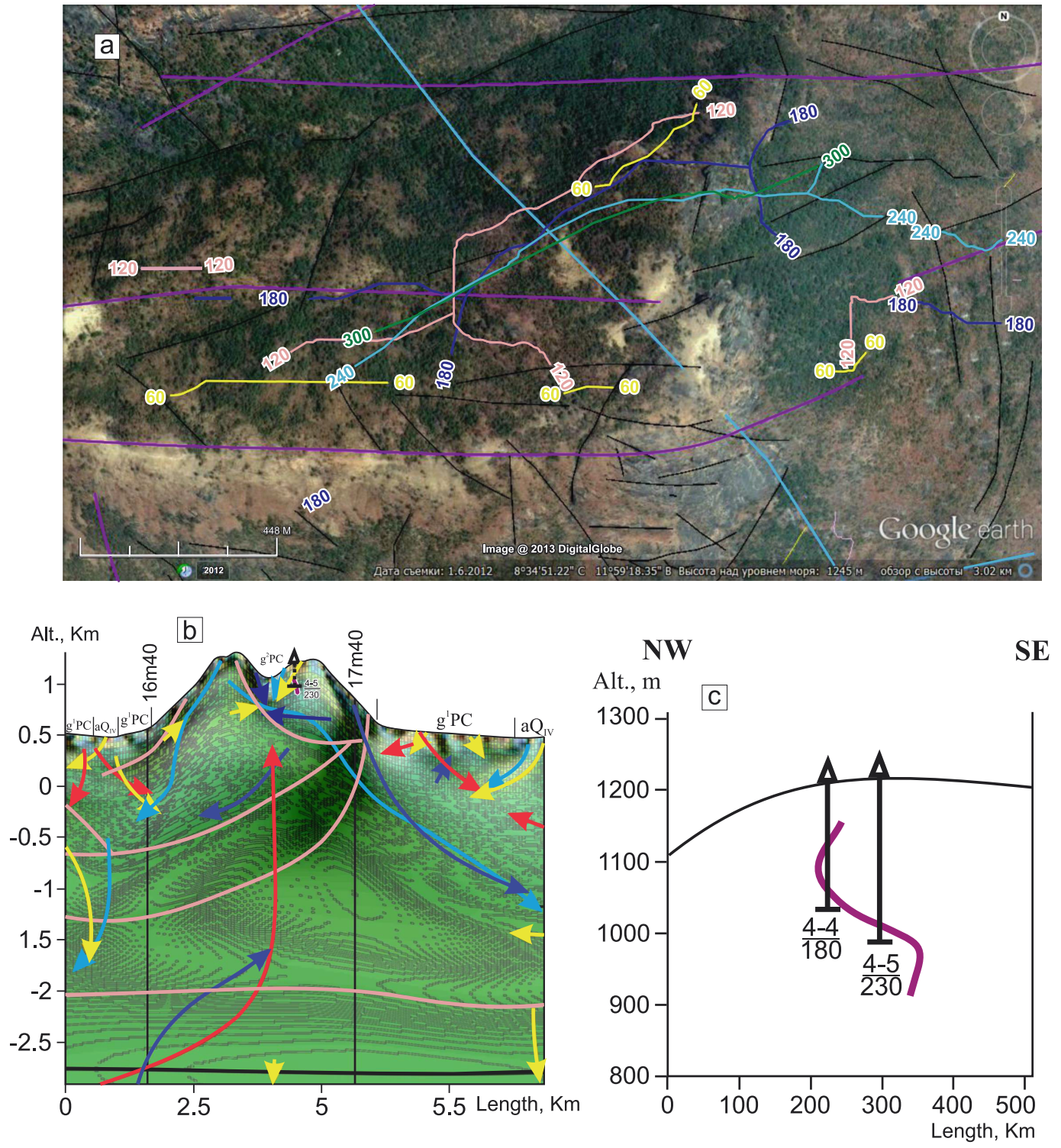

Fig. 14. (a) Spatial distribution of the Zeibei ore body (PBF2) at depths of 60–300 m, overlaid on Google Earth imagery with decoded lineaments: black (Google-derived), crimson (Landsat Band 6 thermal anomalies), and blue (Landsat water-saturated channels). Violet segments mark surface fractures indicative of barite mineralization. The deposit evolves from discrete 470 m lineaments (60 m depth; $\nabla T = 0.52 \pm 0.03$ K/m) to a 1,590 m ENE-trending body (180 m depth) with a central meridian, before contracting vertically to 1,110 m at 300 m depth; (b) Cross-section showing depth-dependent reorientation (NNW → SSE → vertical) controlled by steep thermal gradients ($\partial T/\partial z = 0.72$ K/m) and endogenous fluid influx ($\partial^2 T/\partial z^2 = -0.43$ K/m^2); (c) Recommended drillholes (4–4/180 m, 4–5/230 m) targeting high-gradient zones ($|\nabla T| > 0.8$ K/m) and fluid-saturated fractures (W > 0.3), with confirmatory holes probing vertical structures below 300 m. All align with NNW fault trends (800–1300 m ASL).

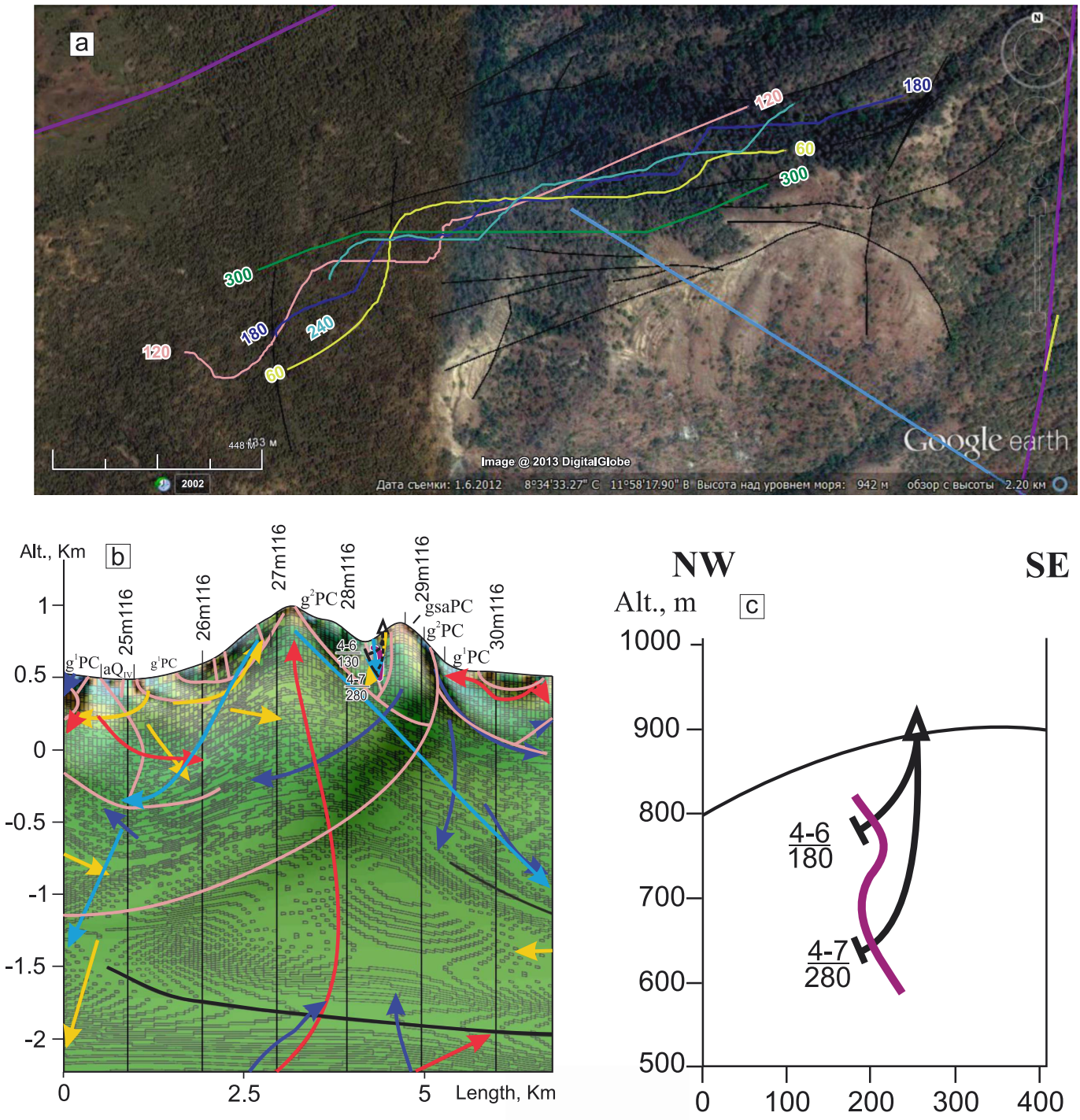

Fig. 15. (a) Spatial distribution of the Ngurore ore body (60–300 m depth) overlain on Google Earth imagery with decoded lineaments: black (Google-derived), crimson (Landsat Band 6 thermal anomalies), and blue (Landsat water-saturated channels). The deposit exhibits a propeller-like geometry, expanding from 870 m (60 m depth) to 1,000 m (120–180 m depth) before contracting to 780 m (300 m depth), with LT algorithm-detected endogenous fluid signatures (Td < 0.08 W/m^2, W > 0.3) at depth; (b) cross-section revealing near-vertical mineralization controlled by thermal–hydrological anomalies (∇T > 0.7 K/m) along NNW–SE fractures; (c) proposed 410 m drilling program (two 205 m holes) targeting peak gradient zones (180–240 m: ∇T > 0.7 K/m, W > 0.3) and mineralization boundaries (300 m: ∂T/∂z > 0.8 K/m) to validate the propeller-shaped ore body.

WNW dip) that expand from 610 m (60 m depth) to 2,360 m (180 m, including the northern branch) and then contract to 750 m (300 m; Fig. 13b). Surface expressions are absent, although potential outcrops may exist at the watershed crest. Thermodynamic analysis revealed control by dry descending vectors and AICDS-mapped fractures (Fig. 13c). The VT algorithm prioritized the 120 m slice (|∇T| > 0.8; Fig. 13d), revealing ΔT ≈ 0.08 K anomalies (SNR ~ 2,000:1) extending to a depth of 1,800 m. The three proposed drillholes (totalling 620 m; Fig. 13d) target distinct features: hole 4–1 (140 m depth) investigates shallow thermal anomalies (ΔT ≈ 0.08 K), hole 4–2 (200 m) tests the mineralized boundary marked by fluid influx indicators (∂W/∂z > 0.1 m^{-1}), and hole 4–3 (280 m) probes deep inflection zones (∂^{2}T/∂z^2 < −0.3 K/m^2) potentially hosting barite-bearing fractures.

The Yebbe deposit occurs in Precambrian banded granitoids (1080–

920 m ASL) with ENE-trending mineralization (35° WNW dip) that expands from 610 m (60 m depth) to 1,640 m (120 m) and then contracts to 750 m (300 m; Fig. 13b). AICDS-decoded fractures and descending dry vectors control veins (Fig. 13c). VT algorithm analysis at 120 m depth ($|\nabla T| > 0.8$; Fig. 13d) revealed $\Delta T \approx 0.08$ K anomalies (SNR ~ 2,000:1) extending to 1,800 m. Three recommended 206 m drillholes (Fig. 13d) target: 4–1 (140 m) for shallow $\Delta T \approx 0.08$ K anomalies, 4–2 (200 m) for the mineralized boundary ($\partial W/\partial z > 0.1$ m^{-1}), and 4–3 (280 m) for deep inflection zones ($\partial^2 T/\partial z^2 < -0.3$ K/m^2). All these faults align with NNW faults and 500–1000 m elevation breaks (Fig. 13d).

The Zeibei deposit (1,250 m ASL) occurs in Precambrian granitoids with metasedimentary xenoliths, showing surface fractures potentially indicating barite (Fig. 14a, violet). AICDS analysis reveals depth-dependent evolution: discrete 470 m lineaments at 60 m depth ($\nabla T = 0.52 \pm 0.03$ K/m; $W = 0.18 \pm 0.02$) merge into a 1,480 m ENE-trending body at 120 m depth, expanding to 1,590 m at 180 m with the central meridian (Fig. 14a). The VT algorithm prioritized this zone ($Si = 1.8$) on the basis of steep gradients (0.82 K/m) and curvature (-0.42 K/m^2). The orientation shifts from NNW-slanted (60–120 m) to SSE-slanted (120–180 m), becoming vertical at 240–300 m (1,470 m at 240 m; 1,110 m at 300 m; Fig. 14b). The 1VD/2VD derivatives confirm vertical reorientation at 240 m ($\partial T/\partial z = 0.72$ K/m; $\partial^2 T/\partial z^2 = -0.43$ K/m^2), which coincides with endogenous fluids from depths of 0.8–4 km (Fig. 14b). Four production holes (205 m each; 4–4/180, 4–5/230) target high-gradient zones ($|\nabla T| > 0.8$ K/m) and fluid-saturated fractures ($W > 0.3$), whereas two confirmatory holes (410 m total) validate vertical structures below 300 m ($\partial^2 T/\partial z^2 < -0.4$ K/m^2) and ENE mineralization, all of which are aligned with NNW faults and 800–1,300 m elevation breaks (Fig. 14c).

The Ngurore deposit, adjacent to Zeibei on the western mountain flank, formed a compact near-vertical mineralization with a propeller-like geometry within Precambrian granitoids. Although surface expressions are absent (Fig. 15a), dimensional evolution occurs with depth: extending 870 m at 60 m, expanding to 1,000 m at 120 m, maintaining a length with an ENE slant at 180 m, and then contracting to 750 m at 240 m before slight extension to 780 m at 300 m depth (Fig. 15a). The LT algorithm detected endogenous fluid signatures at the terrain base, which were correlated with low thermal-radiation density ($Td < 0.08$ W/m2) and high water saturation ($W > 0.3$) in deeper zones (Fig. 15a). Vertical sections confirm these endogenous inputs near the plain's geological boundary (Fig. 15b), revealing key formation mechanisms. A 410 m drilling program (two 205 m holes; Fig. 15c) is proposed to investigate (1) the 180–240 m interval with peak thermal gradients ($\nabla T > 0.7$ K/m) and water saturation ($W > 0.3$) and (2) the 300 m vertical transition zone ($\partial T/\partial z > 0.8$ K/m) marking mineralization boundaries. These holes, which are aligned with NNW–SE fractures, validate both the propeller-shaped ore body geometry and its thermal–hydrological system (Fig. 15c). This integrated approach demonstrates the effectiveness of the multichannel algorithm in characterizing complex deposits while providing a framework for resource evaluation.

Taken together, PBF1 (Taso/Tola) shows optimal targets at 180–300 m depths with sharp thermal boundaries ($\partial T/\partial z > 0.6$ K/m; $\partial^2 T/\partial z^2 < -0.3$ K/m^2) and fracture-controlled fluids, as confirmed by drillholes 2–4/220 and 2–5/300 (Table 4). PBF2 (Yebbe/Zeibei/Ngurore) mineralization occurs at 60–300 m, characterized by high-gradient zones ($|\nabla T| > 0.8$ K/m) and endogenous fluids ($W > 0.3$), featuring Yebbe's ENE veins (120 m), Zeibei's vertical reorientation (240 m), and Ngurore's propeller-shaped body (60–300 m). This depth range mirrors global analogues, such as the Red Dog (Alaska) and Meggen (Germany) barite deposits at 300–500 m depths, controlled by faults and hydrothermal processes (Large and Walcher, 1999; Leach et al., 2005). Comparable deep systems also include Mississippi Valley-Type (MVT) deposits (>500 m, up to ~ 1800 m in California) with fault-driven fluids (Hein et al., 2007; Sangster, 1990). Overall, these findings establish a depth-stratified model of barite mineralization, reconciling shallow fracture-controlled deposits with deeper hydrothermal systems, while validating thermal and structural criteria for targeted exploration.

6. Conclusion

This study demonstrates the effectiveness of integrating Landsat-7 ETM + TIR data, SRTM elevation models, and the Thermal Generalization Method (TGM) for subsurface barite exploration in the Eastern Nigerian Basement Terrane. Two previously undefined mineralized systems—PBF1 (Taso–Tola) and PBF2 (Jada–Ganye)—were delineated, each displaying distinct thermal, hydrological, and structural characteristics.

PBF1, hosted in granite–gneiss, is marked by sharp thermal anomalies ($\nabla T > 0.5$ K/m; $\partial^2 T/\partial z^2 < -0.3$ K/m^2), high water saturation (70–90 %), and robust anomalies at 180–300 m depth ($\Delta T = 1.2$ K; SNR 2000:1), confirming exothermic barite precipitation at 60–80 °C. Its mineralization is structurally controlled by ENE lineaments and fracture zones up to 540 m, with persistence to ~ 1,200 m, though beyond optimal depths. By contrast, PBF2, hosted in syn- to post-tectonic granites, exhibits subdued thermal anomalies (40–60 °C) and moderate water saturation (50–70 %), with mineralization localized at 60–300 m along NW–SE compressive structures. Despite weaker signals at depth ($\Delta T = 0.08$ K at 1,800 m), its geometry—uplift blocks, reoriented zones, and propeller structures—highlights structural control on hydrothermal fluid pathways.

Collectively, both fields show that barite deposition is strongly governed by NW–SE compressive stress and enhanced by heat–fluid coupling, with optimal, exploitable mineralization confined to 60–300 m. Importantly, all anomalies exceeded Landsat's thermal resolution thresholds by over three orders of magnitude, providing a robust confidence framework.

This work establishes TGM-decoded TIR as a powerful, non-invasive tool for detecting high-purity, API-compliant barite reserves at depths far exceeding artisanal mining limits (<15 m). Beyond advancing Nigeria's barite exploration, the approach offers a transferable framework for targeting subsurface mineralization in basement and sedimentary terranes globally, contributing to more efficient, cost-effective, and sustainable resource development.

Declaration of competing interest

The authors declare that they have no known competing financial interests or personal relationships that could have appeared to influence the work reported in this paper.

Acknowledgement

We gratefully acknowledge the Institute of Aerospace Instrumentation (IASI-CJSC), Kazan, Russia, for providing the Landsat satellite imagery used in this study. This research was funded by the Adamawa State Government, Nigeria, through the State Ministry of Mineral Resources, Yola (Contract No. 001), and the United Arab Emirates University (UPAR grant no: G00004980-12S218). We thank the Editor-in-Chief, Prof. Huayong Chen, for his editorial handling of the manuscript. We also wish to express our sincere appreciation to the Associate Editor, Prof. Harald G. Dill, and the anonymous Reviewer for their constructive and insightful comments, which have greatly enhanced the quality of this manuscript. The first author also acknowledges the financial support of the Chinese Government Scholarship (CSC, 2021-2025) for his PhD studies.

Appendix A. Supplementary data

Supplementary data to this article can be found online at https://doi.org/10.1016/j.oregeorev.2025.106935.

Data availability

Data will be made available on request.

References

Abraham, E.I., Bayode, B.L., Olubambi, P.A., Adetunji, A.R., Onwualu, A.P., 2021. Characterization of barite ores from selected locations in Nigeria for drilling fluid formulation. Sci. Afr. 14, e01057.

Adebiyi, L.S., Eluwole, A.B., Fajana, A.O., Salawu, N.B., Saleh, A., 2023. Contrasting structures of the Southern Benue trough and the contiguous crystalline basement as observed from high-resolution aeromagnetic data. Sci. Rep. 13 (1), 21516.

Afolayan, D.O., Adetunji, A.R., Onwualu, A.P., Ogolo, O., Amankwah, R.K., 2021. Characterization of barite reserves in Nigeria for use as weighting agent in drilling fluid. J. Pet. Explor. Prod. Technol. 11 (5), 2157–2178.

Ajibade, A.C., Woakes, M., Rahaman, M.A., 1987. Proterozoic crustal development in the Pan-African Regime of Nigeria: Proterozoic Lithospheric. Evolution 17, 259–271.

Ajibade, A.C., Wright, J.B., 1989. The Togo-Benin-Nigeria Shield: evidence of crustal aggregation in the Pan-African belt. Tectonophysics 165 (1–4), 125–129.

Akande, O., Zentelli, M., Reynolds, P.H., 1989. Fluid inclusion and stable isotope studies of Pb-Zn-fluorite-barite mineralization in the lower and middle Benue Trough. Miner. Depos. 24 (3), 183–191.

Andrew-Oha, I., Mosto-Onuoha, K., Sunday-Dada, S., 2017. Contrasting styles of lead-zinc-barium mineralization in the lower Benue Trough. Southeastern Nigeria. Earth Sci. Res. J. 21 (1), 7–16.

Amraoui, T., Ibouh, H., Farah, A., Bammou, Y., Shebl, A., 2025. Remote sensing mapping of structural and hydrothermal alteration in the mougueur inlier, Eastern high atlas. Morocco. Sci. Rep. 15 (1), 14982.

Apeh, O.I., Tenzer, R., Pham, L.T., Ghomsi, F. E. K., Ribeiro-Filho, N., 2024. New insights into crustal and geological structures beneath the Southern Benue trough of Nigeria and parts of Cameroon Volcanic Line from tailored gravity data. Phys. Chem. Earth. Parts A/B/C, 133, 103540.Augier, R., Jolivet, L., couto, D.D., Negro, F., 2013. From ductile to brittle, late-to post-orogenic evolution of the Betic Cordillera: Structural insights from the northeastern Internal zones. Bulletin de la Société Géologique de France, 184(4–5), 405–425.

Owono, F.M., Akoa, P.R.E., Atangana, J.N., 2024. Post Pan-african landscape evolution in the Garoua-Gaschiga Region (North Cameroon, Central Africa): a record of neotectonic, volcanic and climatic controls. Arab. J. Geosci. 17 (3), 110.

Augier, R., Jolivet, L., couto, D.D., Negro, F., 2013. From ductile to brittle, late-to post-orogenic evolution of the Betic Cordillera: Structural insights from the northeastern Internal zones. Bull. Soc. Géol. Fr. 184 (4–5), 405–425.

Barton, C.C., Angelier, J., 2020. Direct Inversion Method of Fault Slip Analysis to Determine the Orientation of principal Stresses and Relative Chronology for Tectonic events in Southwestern White Mountain Region of New Hampshire, USA. Geosciences 10 (11), 464.

Basfar, S., Shokry, A., Iqbal, A., Elkatatny, S., Alajmi, S., 2025. Evaluation of the Effects of Kaolin Clay on the Performance of Barite-Weighted Oil-based Drilling Fluid. ACS Omega 10 (10), 9976–9985.

Behyari, M., Rahimsouri, Y., Hoseinzadeh, E., Kurd, N., 2019. Evaluating of lithological and structural controls on the barite mineralization by using the remote sensing, Fry and fractal methods, Northwest Iran. Arab. J. Geosci. 12, 1–11.

Benkhelil, J., 1989. The origin and evolution of the cretaceous Benue Trough (Nigeria). J. Afr. Earth Sc. 8 (2–4), 251–282.

Blackwell, D., Richards, M., Frone, Z., Batir, J., Ruzo, A., Dingwall, R., Williams, M., 2011. Temperature-at-Depth Maps for the Conterminous US and Geothermal Resource Estimates, No. GRC1029452. Southern Methodist University Geothermal Laboratory, Dallas, TX (United States).

Bogatkin, V.I., Gataullin, R.N., Mukhamedyarov, R., 2011. Selection of Sakhalin Island GRES construction site using MWM technology. Tatarstan Power Industry 4, 48–51. In Russian.

Bruguier, O., Dada, S., Lancelot, J.R., 1994. Early Archaean component (> 3.5 Ga) within a 3.05 Ga orthogneiss from northern Nigeria: U-Pb zircon evidence. Earth Planet. Sci. Lett. 125 (1–4), 89–103.

Bute, I., Yang, X., Cao, J., Liu, L., Deng, J., Haruna, I.V., Girei, M.B., Abubakar, S., Akhtar, S., 2020. Origin and tectonic implications of ferroan alkali-calcic granitoids from the Hawal Massif, east-eastern Nigeria terrane: clues from geochemistry and zircon U-Pb-Hf isotopes. Int. Geol. Rev. 62 (2), 129–152.

Bute, S.I., Yang, X., Yang, X., Girei, M.B., Kayode, A.A., Lu, Y., 2022. Geochemistry, zircon U–Pb ages and Hf isotopes of granites and pegmatites from Gubrunde region in the Eastern Nigeria Terrane: Insight into magmatism and tectonic evolution of the late Pan-african orogeny. Geochemistry 82 (1), 125809.

Calvin, W.M., Littlefield, E.F., Kratt, C., 2015. Remote sensing of geothermal-related minerals for resource exploration in Nevada. Geothermics 53, 517–526.

Chao, J., Zhao, Z., Xu, S., Lai, Z., Liu, J., Zhao, F., Chen, Q., 2024. Geothermal target detection integrating multi-source and multi-temporal thermal infrared data. Ore Geol. Rev. 167, 105991.

Ciullo, P.A., 1996. The industrial minerals. Industrial Minerals and Their Uses 17–82.

Cox, S.F., 2020. The Dynamics of Permeability Enhancement and Fluid Flow in Overpressured, Fracture-Controlled Hydrothermal Systems. In Applied Structural Geology Of Ore-Forming Hydrothermal Systems, Eds, Julie V. Rowland, David A. Rhys. Reviews in Economic Geology, 21.

Dada, S.S., 2008. Proterozoic evolution of the Nigeria–Boborema province. Geol. Soc. Spec. Publ. 294, 121–136.

Dada, S.S., Olobaniyi, S.B., Oha, I.A., Goki, N.G., Salawu, N.B., Ibe, C.U., Garba, A.A., 2024. Crustal Evolution and the Nigerian Metallogenic Framework. CRC Press.

Dada, S.S., Respaut, J.P., 1989. La monzonite à fayalite de Bauchi (Bauchite, nouveau témoin d'un magmatisme suntectonique pan-africain au nord du Nigeria: Comptes rendus de l'Académie des sciences: Série 2. Mécanique, Physique, Chimie, Sciences De L'univers, Sciences De La Terre 309, 887–892.

Dada, S.S., Tubosun, I.A., Lancelot, J.R., Lar, A.U., 1993. Late Archaean U-Pb age for the reactivated basement of Northeastern Nigeria. J. Afr. Earth Sc. 16, 405–412.

Daoud, A.M., Shebl, A., Abdelkader, M.M., Mohieldain, A.A., Csámer, Á., Satti, A.M., Rózsa, P., 2025. Remote sensing and gravity investigations for barite detection in Neoproterozoic rocks in the Ariab area, Red Sea Hills, Sudan. Remote Sens. Appl.: Soc. Environ. 37, 101416.

Dawaï, D., Bouchez, J.L., Paquette, J.L., Tchameni, R., 2013. The Pan-african quartz-syenite of Guider (north-Cameroon): magnetic fabric and U–Pb dating of a late-orogenic emplacement. Precambr. Res. 236, 132–144.

Dill, H.G., Techmer, A., Botz, R., Weber, B., 2012a. Chemical and mineralogical variations at the transition from subaqueous to subaerial rift-related freshwater limestones along the Dead Sea Transform Fault, NW Jordan. Z. Dtsch. Ges. Für Geowiss. 163 (1), 91.

Dill, H.G., Škoda, R., Weber, B., Berner, Z.A., Müller, A., Bakker, R.J., 2012b. A newly discovered swarm of shear-zone-hosted Bi–As–Fe–Mg–P-rich aplites and pegmatites in the Hagendorf–Pleystein pegmatite province, southeastern Germany: a step closer to the metamorphic root of pegmatites. Can. Mineral. 50 (4), 943–974.

Dobretsov, N.L., Koulakov, I.Y., Polyansky, O.P., 2013. Geodynamics and stress–strain patterns in different tectonic settings. Russ. Geol. Geophys. 54 (4), 357–380.

Dora, M.L., Roy, S.K., Khan, M., Randive, K., Kanungo, D.R., Barik, R., Mayachar, G.K., 2022. Rift-induced structurally controlled hydrothermal barite veins in 1.6 Ga granite, Western Bastar Craton, Central India: Constraints from fluid inclusions, REE geochemistry, sulfur and strontium isotopes studies. Ore Geol. Rev. 148, 105050.

Ebunu, A.I., Olanrewaju, Y. A., Ogolo, O., Adetunji, A.R., Onwualu, A.P., 2021. Barite as an industrial mineral in Nigeria: occurrence, utilization, challenges and future prospects. Heliyon, 7(6). e07365. Elrasheed, A.A., Rozsa, P., 2024. Landsat 8 and Sentinel 2 for Detecting Hydrothermal Barite Deposits in Red Sea Hills, Sudan. Conference: XV. GIS Conference and Exhibition. Debrecen, Hungary. 91–98.

Ene, G.E., Okogbue, C.O., 2016. Geological and geotechnical assessment of some derelict barite fields in the Abakaliki Basin. Nigeria. Environ. Earth Sci. 75 (21), 1419.

Ene, G.E., Okogbue, C.O., 2012. Occurrence and industrial properties of some barite deposits in the Abakaliki Basin. Southeastern Nigeria. Nat. Resour. Res. 21 (3), 347–357.

Essalhi, A., Essalhi, M., Toummite, A., 2016. Environmental impact of mining exploitation: a case study of some mines of barite in the Eastern Anti-Atlas of Morocco. J. Environ. Prot. 7 (11), 1473.

Ferré, E.C., Caby, R., 2007. Granulite facies metamorphism and charnockite plutonism: examples from the Neoproterozoic Belt of northern Nigeria. Proc. Geol. Assoc. 118 (1), 47–54.

Ferré, E.C., Caby, R., Peucat, J.J., Capdevila, R., Monié, P., 1998. Pan-african, post-collisional, ferro-potassic granite and quartz–monzonite plutons of Eastern Nigeria. Lithos 45 (1–4), 255–279.

Ferré, E.C., Deleris, J., Bouchez, J.L., Lar, A.V., Peucat, J.J., 1996. The Pan-african reactivation of contrasted Eburnean and Archaean provinces in Nigeria: structural and isotopic data. J. Geol. Soc. London 153, 719–728.

Ferré, E., Gleizes, G., Caby, R., 2002. Obliquely convergent tectonics and granite emplacement in the Trans-Saharan belt of Eastern Nigeria: a synthesis. Precambr. Res. 114 (3–4), 199–219.

Gajere, J.N., Adekeye, O.A., Tende, A.W., Aminu, M.D., 2024. GIS-based multi-criteria decision models for barite exploration in Nigeria's Benue Trough. Sci. Rep. 14 (1), 14031.

Griffith, E.M., Paytan, A., 2012. Barite in the ocean–occurrence, geochemistry and palaeoceanographic applications. Sedimentology 59 (6), 1817–1835.

Guiraud, M., Ajakaiye, D.E., Ugodulunwa, F.X.O., 1989. Characterisation of late cretaceous NE-SW sinistral wrench faults in the upper Benue Trough (Nigeria) using microtectonic and aeromagnetic data. J. Afr. Earth Sc. 9 (1), 9–21.

Hanor, J.S., 2000. Barite–celestine geochemistry and environments of formation. Rev. Mineral. Geochem. 40 (1), 193–275.

Halilu, M., Haruna, A.I., Abdullahi, F., Ahmed, M.S., Kamaunji, V.D., Girei, M.B., Sanislav., I.V., Lasheen, E.R., Sami, M., 2025. Petrogenesis of migmatites from Liman Katagum area (Bauchi) North-East Nigeria: Constraints from U-Pb and Lu-Hf isotopic data. J. Afr. Earth Sci. 224, 105562.

Hanor, J.S., 1969. Barite saturation in sea water. Geochim. Cosmochim. Acta 33 (7), 894–898.

Henkel, S., Mogollón, J.M., Nöthen, K., Franke, C., Bogus, K., Robin, E., Bahr, A., Blumenberg, M., Pape, T., Seifert, R., März, C., de Lange, G.J., Kasten, S., 2012. Diagenetic barium cycling in Black Sea sediments–a case study for anoxic marine environments. Geochim. Cosmochim. Acta 88, 88–105.

Hein, J.R., Zierenberg, R.A., Maynard, J.B., Hannington, M.D., 2007. Barite-forming environments along a rifted continental margin, Southern California Borderland. Deep Sea Res. Part II 54 (11–13), 1327–1349.

Hong, M., Dai, L., Hu, H., Zhang, X., Li, C., 2022. High-temperature and high-pressure phase transition of natural barite investigated by Raman spectroscopy and electrical conductivity. Front. Earth Sci. 10, 864183.

Irvine, T.N., 1989. A global convection framework; concepts of symmetry, stratification, and system in the Earth's dynamic structure. Econ. Geol. 84 (8), 2059–2114.

Jaupart, C., Mareschal, J.C., 2007. Heat Flow and thermal Structure of the Lithosphere. In: Schubert, G. (Ed.), Treatise Geophys. Elsevier, Oxford, pp. 217–252.

Kamaunji, V.D., Kamaunji, D.Z., Gana, V., Ntekim, E.E., Ukaomah, C.F., Madaki, A.I., 2022a. Integrated Landsat multispectral imagery and airborne geophysical data for

enhanced litho-structural mapping: a case study of Adamawa Massif, north-eastern Nigeria. J. Afr. Earth Sc. 195, 104677.
Kamaunji, V.D., Kamaunji, D.Z., Ntekim, E.E., Ahmed, H.A., Madaki, A.I., Vincent, V. I., Ukaomah, C.F., 2021. Genesis and quality assessment of flake graphites in Toungo area, Adamawa Massif, northeastern Nigeria. Arab. J. Geosci. 14(15), 1532, 1–19.
Kamaunji, V.D., Wang, L.X., Ahmed, H.A., Zhu, Y.X., Vincent, V.I., Girei, M.B., 2020. Coexisting A1 and A2 granites of Kudaru complex: implications for genetic and tectonic diversity of a-type granite in the Younger Granite province, north-central Nigeria. Int. J. Earth Sci. 109, 511–535.
Kamaunji, V.D., Wang, L.X., Chen, W., Girei, M.B., Ahmed, H.A., Zhu, Y.X., Vincent, V.I., Cao, L., 2023. Petrogenesis and rare-metal mineralization of the Ririwai alkaline granitoids, north-central Nigeria: mineralogical and geochemical constraints. Int. Geol. Rev. 66 (13), 2409–2439.
Kamaunji, V.D., Wang, L., Girei, M.B., Zhu, Y., Li, L., Vincent, V.I., Amuda, A.K., 2022b. Petrogenesis and tectonic implication of the alkaline ferroan granites from Ropp complex, north-central Nigeria: Clues from zircon chemistry, U–Pb dating, and Lu–Hf isotope. Geol. J. 58 (1), 21–50.
Kamaunji, V.D., Wang, L.X., Thomas Murphy, D., Girei, M.B., Abba Ahmed, H., Fatima Etsu, B., Sami, M., 2024. Petrogenesis and tectonic implications of peralkaline-metaluminous magmatism in Kila and Shira ring complexes, north-central Nigeria. Int. Geol. Rev. 67 (10), 1279–1305.
Kastner, M., Siever, R., 1983. Siliceous sediments of the Guaymas Basin: the effect of high thermal gradients on diagenesis. J. Geol. 91 (6), 629–641.
Klee, J., Chabani, A., Ledésert, B.A., Potel, S., Hébert, R.L., Trullenque, G., 2021. Fluid-rock interactions in a paleo-geothermal reservoir (Noble Hills Granite, California, USA). part 2: the influence of fracturing on granite alteration processes and fluid circulation at low to moderate regional strain. Geosciences, 11(11), 433.
Kronyak, R.E., Kah, L.C., Edgett, K.S., VanBommel, S.J., Thompson, L.M., Wiens, R.C., Sun, V.Z., Nachon, M., 2019. Mineral-filled fractures as indicators of multigenerational fluid flow in the Pahrump Hills member of the Murray formation, Gale crater. Mars. Earth Space Sci. 6 (2), 238–265.
Labe, N.A., Ogunleye, P.O., Ibrahim, A.A., 2018. Field occurrence and geochemical characteristics of the baryte mineralization in Lessel and Ihugh areas, lower Benue Trough, Nigeria. J. Afr. Earth Sci. 142, 207–217.Large, D., Walcher, E., 1999. the Rammelsberg massive sulphide Cu-Zn-Pb-Ba-Deposit, Germany: an example of sediment-hosted, massive sulphide mineralisation. Miner. Deposita 34, 522–538.
Leach, D.L., Sangster, D.F., Kelley, K.D., Large, R.R., Garven, G., Allen, C.R., Gutzmer, J., and Walters, S., 2005, Sediment-hosted lead-zinc deposits: A global perspective in Hedenquist, J.W., Thompson, J.F.H., Goldfarb, R.J., and Richards, J.P., eds., Economic Geology 100th Anniversary Volume: Littleton, CO, SEG, 561–607.
Large, D., Walcher, E., 1999. The Rammelsberg massive sulphide Cu-Zn-Pb-Ba-Deposit, Germany: an example of sediment-hosted, massive sulphide mineralisation. Miner. Deposita 34 (5), 522–538.
Li, C., Guo, N., Li, Y., Luo, H., Zhuo, Y., Deng, S., Li, X., 2025. Enhancing Geothermal Anomaly Detection with Multi-Source thermal Infrared Data: a Case of the Yangbajing–Yangyi Basin. Tibet. Appl. Sci. 15 (7), 3740.
Liégeois, J.P., 2019. A new synthetic geological map of the Tuareg Shield: An overview of its global structure and geological evolution. In: Bendaoud, A., Hamimi, Z., Hamoudi, M., Djemai, S., Zoheir, B. (Eds.), The geology of the Arab world-an overview. Springer Geology, Switzerland, pp. 83–107.
Madani, A.A., Said, S.M., 2024. Satellite land surface temperature for mapping the structurally controlled geothermal anomalies in the cretaceous rift. South Egypt. NRIAG J. Astron. Geophys. 13 (1), 141–152.
Mahboob, M.A., Celik, T., Genc, B., 2024. Predictive modelling of mineral prospectivity using satellite remote sensing and machine learning algorithms. Remote Sens. Appl.: Soc. Environ. 36, 101316.
Maurin, J.C., Benkhelil, J., 1990. Model of Pb/Zn mineralization genesis in the cretaceous Benue Trough (Nigeria): Structural, geophysical and geochemical constraints. J. Afr. Earth Sc. 11 (3–4), 345–349.
Maurin, J.C., Benkhelil, J., Robineau, B., 1986. Fault rocks of the Kaltungo lineament, NE Nigeria, and their relationship with Benue Trough tectonics. J. Geol. Soc. 143 (4), 587–599.
McCurry, P., 1971. Pan-african orogeny in northern Nigeria. Geol. Soc. Am. Bull. 82 (11), 3251–3262.
Melekestseva, I.Y., Tret'yakov, G.A., Nimis, P., Yuminov, A.M., Maslennikov, V.V., Maslennikova, S.P., Maslennikova, S.P., Kotlyarov, V.A., Beltenev, V.E., Danyushevsky, L.V., Large, R., 2014. Barite-rich massive sulfides from the Semenov-1 hydrothermal field (Mid-Atlantic Ridge, 13 30.87′ N): evidence for phase separation and magmatic input. Mar. Geol. 349, 37–54.
Ministry of Commerce, n.d.. Industries and Solid Minerals Development (MCISMD, 2004). Geology and Mineral Resources of Adamawa State (Handbook). p. 21p.
Ministry of Mines and Steel Development (MMSD), 2018. www.minesandsteel.gov.ng. Nigeria Geological Survey Agency, 2011. Mineral Resources Inventory of Gold. Barites, Gypsum and Bentonite.
Mukhamedyarov, R.D., 1993. Deterministic synthesis of optical-electronic systems with symmetric input. Optical Magazine 9, 34–58.
Mukhamedyarov, R.D., 2002. The method of video thermal and generalization of its aerospace equipment. Interval 9 (44), 59–62. In Russian.
Mukhamedyarov, R.D., 2006. "Eye of the Earth"- aerospace monitoring system. Aerospace Courier 3 (45), 44–45. In Russian.
Mukhamedyarov R.D., 2008. Method of video-thermal imaging generalization of aerospace surveys for solving geoanthropogenic tasks. Report collection. V international science-practical conference (Urgent problems of uranium industry), Almaty, 319–334 (In Russian).
Mukhamedyarov, R.D., 2010a. Project "All-Seeing Eye"-an Earth monitoring Aerospace System. current issues in Aviation and Aerospace Systems: Processes. Models, Experiment. 15 (1). 1(30), 33–40. In Russian.
Mukhamedyarov, R.D., 2010b. Solution to energy challenges in geointroscopy based on video-thermal generalization technology for aerospace and terrestrial imaging. New Technologies and Scientific-Technical Developments in Energy. Institute of Aerospace Instrumentation 15(1), 30, 17–25. In Russian.
Mukhamedyarov, R.D., 2011. Solution of Energy Problems of Geointrosopy based on Technology Method of Video thermal Generalization of Aerospace and Ground Images. Energy of Tartastan 3, 17–25. In Russian.
Mukhamedyarov, R.D., 2012. Video-thermal generalization method and its geotechnogenic significance. Bulletin of KNRTU 1, 60–66. In Russian.
Mukhamedyarov, R.D., 2013. Final Report Satellite Mineral Survey in Adamawa State (contract no. 001) conducted by CJSC "The Institute for Aerospace Instrumentation" Russian Federation, 420075, Kazan. Submitted to the Ministry of Mineral Resources, Yola, Adamawa State, Nigeria. 313p.
Mukhamedyarov, R.D., 2016. The All-Seeing Eye of Space, in: New Technologies, Materials and Equipment of the Russian Air Space Industry–AKTO 2016. Academy of Sciences of the Republic of Tatarstan, Kazan, 870–878 (In Russian).
Moles, N.R., Boyce, A.J., Warke, M.R., Claire, M.W., 2024. Syn-sedimentary exhalative or diagenetic replacement? Multi-proxy evidence for origin of metamorphosed stratiform barite–sulfide deposits near Aberfeldy. Scottish Highlands. Minerals 14 (9), 865.
Nait-Bba, A., Aabi, A., Samaoui, S., Hejja, Y., Baidder, L., Boujamaoui, M., Jilali, A., Rezouki, I., 2024. Tectonic pattern and relative age of Ba-rich veins in front of a poly-deformed Precambrian inlier (Saghro, Morocco). J. Iber. Geol. 50 (2), 157–175.
Nash, G.D., 1996. Applications of remote sensing and geographic information systems as geothermal exploration tools in the Great Basin, United States of America. The University of Utah ProQuest Dissertations & Theses 9639776, 125p.
Ngako, V., Njonfang, E., Aka, F.T., Affaton, P., Nnange, J.M., 2006. The North–South Paleozoic to Quaternary trend of alkaline magmatism from Niger–Nigeria to Cameroon: complex interaction between hotspots and Precambrian faults. J. Afr. Earth Sci. 45 (3), 241–256.
Nigeria Geological Survey Agency (NGSA), 2011. Mineral Resources Inventory of Gold. Barites, Gypsum and Bentonite.
Obaje, N.G., 2009. Geology and Mineral Resources of Nigeria. In: Bhattacharji, S., Neugebauer, H.J., Reitner, J., Stüwe, K. (Eds.), Lecture Notes in Earth Sciences, vol 1. Springer, Berlin, Heidelberg, XIV, p. 221.
O'Driscoll, M.O., 2017. Barite miners in Nigeria receive a government boost; call for import ban to be reinstated. Proceedings from the Industrial Mineral Forums and Research 21–23.
Offodile, M.E., 1976. A review of geology of the cretaceous of the Benue Valley. In: Kogbe, C.A. (Ed.), Geology of Nigeria. Rock View Ltd, Jos, pp. 364–376.
Offodile, M.E., 1989. A Review of the Geology of the Cretaceous Benue Valley. In: Kogbe, C.A. (Ed.), Geology of Nigeria. Elizabethan Publishing Co, Lagos.
Ogundipe, I.E., 2017. Thermal and chemical variations of the Nigerian Benue trough lead-zinc-barite-fluorite deposits. J. Afr. Earth Sc. 132, 72–79.
Oha, I.A., Nnebedum, O.D., Okonkwo, I.A., 2021. Alteration mapping for lead-zinc-barium mineralization in parts of the Southern Benue Trough, Nigeria, using ASTER Multispectral Data. Earth Sci. Res. 10(1), 1–61.Olade, M.A., 1975. Evolution of Nigerian Benue Trough (Aulacogen): a tectonic model. Geol. Mag. 112, 575–583.
Ominigbo, O.E., 2022. Evolution of the Nigerian basement complex: current status and suggestions for future research. J. Min. Geol. 58 (1), 229–236.
Onyeagocha, A.C., Ekwueme, B.N., 1990. Temperature-pressure distribution patterns in metamorphosed rocks of the Nigerian basement complex–a preliminary analysis. J. Afr. Earth Sc. 11 (1–2), 83–93.
Orywall, P., Drüppel, K., Kuhn, D., Kohl, T., Zimmermann, M., Eiche, E., 2017. Flow-through experiments on the interaction of sandstone with Ba-rich fluids at geothermal conditions. Geotherm. Energy 5, 1–24.
Ottan, A.S., Otoijamun, I., Dele, A.A., Onwualu, A.P., 2022. A Review of Exploitation Techniques of Barite Deposits of Nasarawa State. Nigeria. Mater. Sci. 4 (2), 1–l0.
Otoijamun, I., Kigozi, M., Adetunji, A.R., Onwualu, P.A., 2021. Characterization and suitability of Nigerian barites for different industrial applications. Minerals, 11(4), 360.Prakash, A., 2000. Thermal remote sensing: concepts, issues and applications. Int. Arch. Photogramm. Remote Sens. 33(B1; PART 1), 239-243.
Penaye, J., Kröner, A., Toteu, S.F., Van Schmus, W.R., Doumnang, J.C., 2006. Evolution of the Mayo Kebbi region as revealed by zircon dating: an early (ca. 740 Ma) Pan-African magmatic arc in southwestern Chad. J. Afr. Earth Sci. 44 (4–5), 530–542.
Pouclet, A., Vidal, M., Doumnang, J.C., Vicat, J.P., Tchameni, R., 2006. Neoproterozoic crustal evolution in Southern Chad: Pan-African Ocean basin closing, arc accretion and late-to post-orogenic granitic intrusion. J. Afr. Earth Sci. 44 (4–5), 543–560.
Rahaman, M.A., Van Breemen, O., Bowden, P., Bennett, J.N., 1984. Age migrations of anorogenic ring complexes in Northern Nigeria. J. Geol. 92 (2), 173–184.
Rani, K., 2025. Mineral Exploration using Remote Sensing. In: Remote Sensing for Geophysicists. CRC Press, pp. 79–94.
Samaila, N.K., Ekeleme, I.A., Ajol, F.A., Aga, T., Adelabu, A.P., 2025. Baryte Mineralization in Faya Area and Environs, Langtang South, Middle Benue Trough, Northcentral Nigeria: Inferences from Geology, Petrography and Trace element Geochemistry. J. Afr. Earth Sc. 105714.
Samaoui, S., Aabi, A., Nguidi, M.A., Boushaba, A., Belkasmi, M., Baidder, L., Zehni, A., 2023. Fault-controlled barite veins of the eastern Anti-Atlas (Ougnat, Morocco), a far-field effect of the Central Atlantic opening? Structural analysis and metallogenic implications. J. Afr. Earth Sc. 204, 104970.
Samaoui, S., Aabi, A., Boushaba, A., Mohammed, B., Nait Bba, A., Essaifi, A., Lamrani, O., 2024. Metallogeny and Genesis of Fault-filling Barite-Sulfide Veins

(Ougnat, Morocco): Petrography, Fluid Inclusion, and Sr-S Isotopic Constraints. Geosciences 14 (3), 83.
Sangster, D.F., 1990. Mississippi Valley-type and SEDEX lead-zinc deposits: a comparative examination: Institution of Mining and Metallurgy. transactions. Section b: Appl. Earth Sci. 99, 21–42.
Sary, C.A., 2024. Identification of geothermal potential zone associated with land surface temperature derived from Landsat 8 data using split-window algorithm. J. Appl. Res. 22 (1), 125–137.
Schleicher, A.M., Tourscher, S.N., van der Pluijm, B.A., Warr, L.N., 2009. Constraints on mineralization, fluid-rock interaction, and mass transfer during faulting at 2–3 km depth from the SAFOD drill hole. J. Geophys. Res. Solid Earth 114 (B4).
Shellnutt, J.G., Pham, N.H.T., Denyszyn, S.W., Yeh, M.W., Lee, T.Y., 2017. Timing of collisional and post-collisional Pan-African Orogeny silicic magmatism in south-central Chad. Precambrian Res 301, 113–123.
Shellnutt, J.G., Yeh, M.W., Lee, T.Y., Iizuka, Y., Pham, N.H.T., Yang, C.C., 2018. The origin of Late Ediacaran post-collisional granites near the Chad Lineament, Saharan Metacraton, south-central Chad. Lithos 304, 450–467.
Shemang, E.M., Ajayi, C.O., Jacoby, W.R., 2001. A magmatic failed rift beneath the Gongola arm of the upper Benue trough, Nigeria? J. Geodyn. 32 (3), 355–371.
Sunday, O.P., Oluseyi Adunola, B., Thaddeus, I., 2020. Geochemistry, Mineralogy and Petrogenesis of the Vein-Type Barites of some Portions of the Benue Trough. Nigeria. Lithol. Miner. Resour. 55 (6), 528–537.
Sun, Z., Jiang, C., Wang, X., Zhou, W., Lei, Q., 2021. Combined effects of thermal perturbation and in-situ stress on heat transfer in fractured geothermal reservoirs. Rock Mech. Rock Eng. 54, 2165–2181.
Teske, A., 2020. Guaymas Basin, a hydrothermal hydrocarbon seep ecosystem. Microbiology and Biogeochemistry of a Global Marine Habitat, Marine Hydrocarbon Seeps, pp. 43–68.
Torres, M.E., Brumsack, H.J., Bohrmann, G., Emeis, K.C., 1996. Barite fronts in continental margin sediments: a new look at barium remobilization in the zone of sulfate reduction and formation of heavy barites in diagenetic fronts. Chem. Geol. 127 (1–3), 125–139.
Toteu, S.F., Penaye, J., Djomani, Y.P., 2004. Geodynamic evolution of the Pan-african belt in central Africa with special reference to Cameroon. Can. J. Earth Sci. 41 (1), 73–85.
Tranter, M., De Lucia, M., Kühn, M., 2021. Barite scaling potential modelled for fractured-porous geothermal reservoirs. Minerals 11 (11), 1198.
Tumanov, V., 2007. The video thermal generalization method is one of the promising areas of geology research hydrocarbons. Enhanced oil recovery in the late stage of development of. In: natural bitumen. Kazan Publishing house "FEN" S, pp. 580–585.
Tumanov, V., Cheban, V.D., 2013. Application of method of video-thermal generalization for the estimation of hydrocarbon accumulation in the Western desert of Egypt. Oil and Gas Industry of Ukraine 3, 10–16. In Russian.
Turcotte, D.L., Schubert, G., 2014. Geodynamics, 3rd edn. Cambridge University Press, Cambridge, UK, p. 623.
United States Geological Survey (USGS) 2019a. Landsat 7 (L7) Data Users Handbook. [Online]. https://prd-wret.s3.us-west 2.amazonaws.com/assets/palladium/production/atoms/files/LSDS-1927_L7_Data_Users_Handbook-v2.pdf. Accessed 31 May 2025.
U.S. Geological Survey (USGS) 2019b. Landsat Collection 2 Level-1 Product Definition, Data Users' Handbook. URL: https://www.usgs.gov/landsat-missions/landsat-collection-2.
Uma, K.O., 1998. The brine fields of the Benue Trough, Nigeria: a comparative study of geomorphic, tectonic and hydrochemical properties. J. Afr. Earth Sc. 26 (2), 261–275.
United States Geological Survey, (USGS) 2021. U.S. Geological Survey Minerals Yearbook, Ed(s) Mcrae, M.E., Barite [Advanced Release], 9.1–9.12.
Wagner, T., Kirnbauer, T., Boyce, A.J., Fallick, A.E., 2005. Barite–pyrite mineralization of the Wiesbaden thermal spring system, Germany: a 500-kyr record of geochemical evolution. Geofluids 5 (2), 124–139.
Wang, S., Wang, L., Brown, M., Feng, P., 2016. Multi-stage barite crystallization in partially melted UHP eclogite from the Sulu belt. China. American Mineralogist 101 (3), 564–579.
Wang, S., Xu, W., Guo, T., 2024. Advances in thermal infrared remote sensing technology for geothermal resource detection. Remote Sens. 16 (10), 1690.
Wind, S.C., Hannington, M.D., Schneider, D.A., Fietzke, J., Kilias, S.P., Bruce Gemmell, J., 2023. Origin of Hydrothermal Barite in Polymetallic Veins and Carbonate-Hosted Deposits of the Cyclades Continental Back Arc. Econ. Geol. 118 (8), 1959–1994.
Woakes, M., Rahaman, M.A., Ajibade, A.C., 1987. Some metallogenetic features of the Nigerian basement. J. Afr. Earth Sc. 6 (5), 655–664.
Yang, L.L., Wu, Y.P., Liu, Z.Y., Ou, Z.T., Chen, H.Z., Jiang, G.C., Dong, T.F., Yu, C.J., Feng, S.J., 2025. Preparation, characterization and application of modified barite grafted with lipophilic polymers for oil-based drilling fluids. Geoenergy Sci. Eng. 251, 213882.
Yao, W., Tsang, M.Y., Wortmann, U.G., 2022. Oxidation of pyrite during barite extraction. Chem. Geol. 607, 121011.
Zhao, F., Peng, Z., Qian, J., Chu, C., Zhao, Z., Chao, J., Xu, S., 2024. Detection of geothermal potential based on land surface temperature derived from remotely sensed and in-situ data. Geo-Spat. Inf. Sci. 27 (4), 1237–1253.
Zou, H., Zhang, S.T., Chen, A.Q., Fang, Y., Zeng, Z.F., 2016. Hydrothermal fluid sources of the Fengjia barite–fluorite deposit in Southeast Sichuan, China: evidence from fluid inclusions and hydrogen and oxygen isotopes. Resour. Geol. 66 (1), 24–36.
Zuo, L., Wang, G., Carranza, E.J.M., Pang, Z., Ren, H., Cao, K., Gao, M., 2023. Deep Vector Exploration via Alteration Footprints and thermal Infrared Scalars for the Weilasituo Magmatic–Hydrothermal Li–Sn Polymetallic Deposit, Inner Mongolia. NE China. Nat. Resour. Res. 32 (5), 1871–1895.